

# Multi-Scaling Differential Contraction Integral Method for Inverse Scattering Problems with Inhomogeneous Media

Y. Zhong<sup>(1)(2)</sup>, F. Zardi<sup>(3)(4)</sup>, M. Salucci<sup>(3)(4)</sup>, G. Oliveri<sup>(3)(4)</sup>, and A. Massa<sup>(3)(4)(5)(6)</sup>

<sup>(1)</sup> *FINIAC Pte. Ltd.*

JTC LaunchPad @ JID, 2 Cleantech Loop, Singapore, 637144

Email: [zhongyu@fniac.io](mailto:zhongyu@fniac.io)

<sup>(2)</sup> Dept. of Physics and Technology, UiT The Arctic University of Norway

NO-9037 Tromsø, Norway.

Email: [yu.zhong@uit.no](mailto:yu.zhong@uit.no)

<sup>(3)</sup> *ELEDIA Research Center (ELEDIA@UniTN - University of Trento)*

DICAM - Department of Civil, Environmental, and Mechanical Engineering

Via Mesiano 77, 38123 Trento - Italy

E-mail: [{francesco.zardi, marco.salucci, giacomo.oliveri, andrea.massa}@unitn.it](mailto:{francesco.zardi, marco.salucci, giacomo.oliveri, andrea.massa}@unitn.it)

Website: [www.eledia.org/eledia-unitn](http://www.eledia.org/eledia-unitn)

<sup>(4)</sup> *CNIT - "University of Trento" ELEDIA Research Unit*

Via Sommarive 9, 38123 Trento - Italy

Website: [www.eledia.org/eledia-unitn](http://www.eledia.org/eledia-unitn)

<sup>(5)</sup> *ELEDIA Research Center (ELEDIA@UESTC - UESTC)*

School of Electronic Engineering, Chengdu 611731 - China

E-mail: [andrea.massa@uestc.edu.cn](mailto:andrea.massa@uestc.edu.cn)

Website: [www.eledia.org/eledia-uestc](http://www.eledia.org/eledia-uestc)

<sup>(6)</sup> *ELEDIA Research Center (ELEDIA@TSINGHUA - Tsinghua University)*

30 Shuangqing Rd, 100084 Haidian, Beijing - China

E-mail: [andrea.massa@tsinghua.edu.cn](mailto:andrea.massa@tsinghua.edu.cn)

Website: [www.eledia.org/eledia-tsinghua](http://www.eledia.org/eledia-tsinghua)

***This work has been submitted to the IEEE for possible publication. Copyright may be transferred without notice, after which this version may no longer be accessible.***

# Multi-Scaling Differential Contraction Integral Method for Inverse Scattering Problems with Inhomogeneous Media

Y. Zhong, F. Zardi, M. Salucci, G. Oliveri, and A. Massa

## Abstract

Practical applications of microwave imaging often require the solution of inverse scattering problems with inhomogeneous backgrounds. Towards this end, a novel inversion strategy, which combines the multi-scaling (*MS*) regularization scheme and the Difference Contraction Integral Equation (*DCIE*) formulation, is proposed. Such an integrated approach mitigates the non-linearity and the ill-posedness of the problem to obtain reliable high-resolution reconstructions of the unknown scattering profiles. The arising algorithmic implementation, denoted as *MS-DCIE*, does not require the computation of the Green's function of the inhomogeneous background, thus it provides an efficient and effective way to deal with complex scenarios. The performance of the *MS-DCIE* are assessed by means of numerical and experimental tests, in comparison with competitive state-of-the-art inversion strategies, as well.

**Key words:** Microwave Imaging, Inverse Scattering, Multi-Scaling, Difference Contraction Integral Equation, Inhomogeneous Media.

# 1 Introduction

In engineering, microwave imaging applications are concerned with both homogeneous [1]-[30] and inhomogeneous [31]-[50] backgrounds. In both cases, the behavior of time-harmonic electromagnetic fields (*EMs*) and their interactions with the environment (i.e., scatterers, host medium, and receivers) can be faithfully described in terms of either the wave equation, which is a partial differential equation (*PDE*), or the corresponding integral equation (*IE*).

Well-known examples of inverse scattering (*IS*) approaches formulated within the Lippmann-Schwinger *IE* (*LSIE*) are the methods based on the Born [4][5][47], the Rytov [6], and the distorted Born [7][34] approximations or Newton-type techniques [38]. *PDE*-based methods (e.g., [26] and [27]) have been extensively studied, as well. In principle, all these methods can handle *IS* problems (*ISPs*) with inhomogeneous media, but their efficiency and accuracy might be underwhelming since a repeated solution of the corresponding forward scattering problem is required to iteratively update the unknown contrast [28]. Additionally, some approaches rely on linear approximations, which do not hold true for highly-contrasted objects when multiple-scattering phenomena are non-negligible [51].

To avoid multiple calls of a forward solver and to enable the application of different regularization techniques [11][13][22], by also reducing the non-linearity of the *ISP* at hand thanks to new theoretical formulations (e.g., the contraction integral equation (*CIE*) [25][30]) for dealing with strong contrasts or electrically-large scatterers, an alternative class of inversion strategies has been considered. Namely, the modified gradient method [8], the contrast source inversion (*CSI*) method [9], and the subspace-based optimization method (*SOM*) [12][13] have been proposed where the equivalent source is now the “secondary” unknown instead of the *EM* field, while the contrast is still the “primary” quantity to be determined.

To address the *ISPs* with inhomogeneous scenarios, the *CSI* [52] and the *SOM* [53] methods adopt a *PDE*-based modeling for computing the Green’s function of the inhomogeneous background so that the inversion is carried out within the *LSIE* framework. Despite their successful application, these approaches suffer from the heavy computational burden of numerically determining the inhomogeneous-media Green’s function without using acceleration techniques as for homogeneous backgrounds (e.g., the Conjugate Gradient Fast Fourier Transform (*CG-FFT*))

[54] or the Fast Multipole Method (*FMM*) [55]).

Otherwise, the Difference *CIE* (*DCIE*) method [56] exploits an alternative *ISP* formulation that only needs the closed-form expression of the Green's function for the homogeneous background. However, the arising inversion process has to be stabilized [25][30] by means of an effective regularization technique such as the multi-scaling (*MS*) strategy, which has proved able to handle both two-dimensional (*2D*) [51] and three-dimensional (*3D*) [60][61][62] scenarios as well as aspect-limited configurations [63][64]. Moreover, it has been successfully combined with different optimization methods [51][57] and formulations [58][59].

Generally speaking, the *MS* strategy is a multi-zoom meta-level scheme aimed at identifying, at each step, the region of the investigation domain where the unknown scatterers are supposed to be most likely located, referred to as Region of Interest (*RoI*). In this latter, the reconstruction of the objects descriptors, whose number is kept close to the amount of available information from the scattering data/measurements, is then performed with a suitable inversion method. In this way, while mitigating the ill-posedness and the non-linearity of the successive inversions, a multi-resolution imaging of the scenario is yielded, the higher spatial resolution being only in the *RoI* identified at each step.

In this work, the *DCIE* formulation is extended to the *MS* scheme for defining a new inversion strategy able to effectively and efficiently address imaging problems involving unknown objects in inhomogeneous backgrounds. Such an integration is not straightforward since the differential formulation takes into account the *EM* interactions generated by the unknown objects also outside the *RoI*. Indeed, external equivalent currents are generated because of the coupling between unknown scatterers and the inhomogeneous background and they cannot be neglected without compromising the validity of the *IS* model. Therefore, an ad-hoc *RoI* estimation technique is proposed to derive a novel and customized *ISP* solution approach, namely the *MS-DCIE*. This method features the advantages of both the *DCIE* inversion (i.e., computationally fast and weakly non-linear) and the *MS* scheme (i.e., reduced ill-posedness and multi-resolution reconstruction).

The outline of the paper is as follows. The *ISP* is mathematically formulated within the *DCIE* framework in Sect. 2, while Section 3 details the *MS-DCIE* inversion strategy. In Sect. 4, a

representative set of numerical and experimental test cases are presented and discussed to assess the reliability and the effectiveness of the proposed method. Finally, some concluding remarks are drawn (Sect. 5).

## 2 ISP Formulation (DCIE Framework)

Let  $\mathcal{H}$  be a square investigation domain of side  $L_{\mathcal{H}}$  and characterized by a known and inhomogeneous permittivity distribution  $\varepsilon_H(\mathbf{r})$ , which is univocally described by the contrast function  $\tau_H(\mathbf{r}) \triangleq \frac{\varepsilon_H(\mathbf{r})}{\varepsilon_B} - 1$ ,  $\varepsilon_B$  and  $\tau_B(\mathbf{r}) = 0$  being the permittivity and the contrast of the homogeneous external background [Fig. 1(a)], respectively. An unknown scatterer of arbitrary shape and permittivity  $\varepsilon_O(\mathbf{r})$  is located in a region  $\mathcal{O}$  within  $\mathcal{H}$  [Fig. 1(b)] so that the contrast function in  $\mathcal{H}$  turns out to be  $\tau(\mathbf{r}) \triangleq \frac{\varepsilon(\mathbf{r})}{\varepsilon_B} - 1$  (i.e.,  $\tau(\mathbf{r}) = \tau_O(\mathbf{r})$  if  $\mathbf{r} \in \mathcal{O}$ ,  $\tau(\mathbf{r}) = \tau_H(\mathbf{r})$  if  $\mathbf{r} \in \mathcal{H} - \mathcal{O}$ ). The host domain  $\mathcal{H}$  is probed by a transverse magnetic (TM) plane wave from  $V$  different directions  $\{\phi_v; v = 1, \dots, V\}$ ,  $\xi_{inc}^{(v)}$  being the  $z$ -th component of the  $v$ -th ( $v = 1, \dots, V$ ) incident field, and the field  $\xi^{(v)}$  arising from the EM scattering interactions is measured by  $M$  probes located in the observation domain, outside  $\mathcal{H}$ , at the positions  $\{\mathbf{r}_m; m = 1, \dots, M\}$ . By defining the scattered field  $\xi_{sca}^{(v)}$  as  $\xi_{sca}^{(v)} \triangleq \xi^{(v)} - \xi_{inc}^{(v)}$  ( $v = 1, \dots, V$ ), the ISP at hand can be then formulated as the retrieval of the differential contrast  $\tau_{\Delta}$  [ $\tau_{\Delta}(\mathbf{r}) \triangleq \tau(\mathbf{r}) - \tau_H(\mathbf{r})$  - Fig. 1(c)] starting from the knowledge of the measured samples  $\{\xi_{sca}^{(v)}(\mathbf{r}_m); m = 1, \dots, M; v = 1, \dots, V\}$ .

Mathematically, the relation between data and unknowns, subject to the knowledge of the (inhomogeneous) host medium (i.e.,  $\tau_H(\mathbf{r})$ ,  $\mathbf{r} \in \mathcal{H}$ ), is described by the following “differential” version of the LSIE equations

$$\xi_{sca}^{(v)}(\mathbf{r}_m) = \int_{\mathcal{O}} \mathcal{G}_H(\mathbf{r}_m, \mathbf{r}') \tau_{\Delta}(\mathbf{r}') \xi^{(v)}(\mathbf{r}') d\mathbf{r}' \quad (1)$$

$$\xi^{(v)}(\mathbf{r}) = \xi_H^{(v)}(\mathbf{r}) + \int_{\mathcal{O}} \mathcal{G}_H(\mathbf{r}, \mathbf{r}') \tau_{\Delta}(\mathbf{r}') \xi^{(v)}(\mathbf{r}') d\mathbf{r}' \quad (2)$$

where  $\mathcal{G}_H$  is the Green’s function of the inhomogeneous host medium with permittivity  $\varepsilon_H(\mathbf{r})$ , the differential contrast  $\tau_{\Delta}$  is equal to  $\tau_{\Delta}(\mathbf{r}) = \tau_O(\mathbf{r}) - \tau_H(\mathbf{r})$  if  $\mathbf{r} \in \mathcal{O}$ ,  $\tau_{\Delta}(\mathbf{r}) = 0$  otherwise,  $\xi_H^{(v)}$  is the  $v$ -th ( $v = 1, \dots, V$ ) electric field without the object given by

$$\xi_H^{(v)}(\mathbf{r}) = \xi_{inc}^{(v)}(\mathbf{r}) + \int_{\mathcal{H}} \mathcal{G}_B(\mathbf{r}, \mathbf{r}') \tau_H(\mathbf{r}') \xi_H^{(v)}(\mathbf{r}') d\mathbf{r}', \quad (3)$$

$\mathcal{G}_B$  being the Green's function of the background homogeneous medium with permittivity  $\varepsilon_B$ . It is worth noticing that (1)(2) require the evaluation of  $\mathcal{G}_H$ , which can be computationally-demanding.

Alternatively, it is still possible to deduce a “*differential*” *LSIE* formulation (*DLSIE*) without having available  $\mathcal{G}_H$  (see Appendix A)

$$\xi_{sca,\Delta}^{(v)}(\mathbf{r}_m) = \int_{\mathcal{H}} \mathcal{G}_B(\mathbf{r}_m, \mathbf{r}') \left\{ \tau_{\Delta}(\mathbf{r}') \xi^{(v)}(\mathbf{r}') + \tau_H(\mathbf{r}') \left[ \xi^{(v)}(\mathbf{r}') - \xi_H^{(v)}(\mathbf{r}') \right] \right\} d\mathbf{r}' \quad (4)$$

$$\xi^{(v)}(\mathbf{r}) = \xi_H^{(v)}(\mathbf{r}) + \int_{\mathcal{H}} \mathcal{G}_B(\mathbf{r}, \mathbf{r}') \left\{ \tau_{\Delta}(\mathbf{r}') \xi^{(v)}(\mathbf{r}') + \tau_H(\mathbf{r}') \left[ \xi^{(v)}(\mathbf{r}') - \xi_H^{(v)}(\mathbf{r}') \right] \right\} d\mathbf{r}' \quad (5)$$

As a matter of fact, the available information on the host medium is now fully included in (4)(5) through  $\tau_H$  and  $\xi_H^{(v)}$ .

The corresponding differential contrast-source formulation (*DCSIE*) is obtained by multiplying (5) by the contrast function  $\tau$  [9][12] and defining the  $v$ -th ( $v = 1, \dots, V$ ) differential equivalent current  $J_{\Delta}^{(v)}$  as

$$J_{\Delta}^{(v)}(\mathbf{r}) \triangleq J^{(v)}(\mathbf{r}) - J_H^{(v)}(\mathbf{r}), \quad (6)$$

$J^{(v)}$  ( $J_H^{(v)}$ ) being the equivalent current induced on the investigation domain  $\mathcal{H}$  with contrast  $\tau$  ( $\tau_H$ ) and radiating in the free-space background with  $\tau_B(\mathbf{r}) = 0$  [i.e.,  $J^{(v)}(\mathbf{r}) \triangleq \tau(\mathbf{r}) \xi^{(v)}(\mathbf{r})$  and  $J_H^{(v)}(\mathbf{r}) \triangleq \tau_H(\mathbf{r}) \xi_H^{(v)}(\mathbf{r})$ ], so that, after some simple manipulations, it turns out that

$$\xi_{sca,\Delta}^{(v)}(\mathbf{r}_m) = \int_{\mathcal{H}} \mathcal{G}_B(\mathbf{r}_m, \mathbf{r}') J_{\Delta}^{(v)}(\mathbf{r}') d\mathbf{r}' \quad (7)$$

$$J_{\Delta}^{(v)}(\mathbf{r}) = \tau_{\Delta}(\mathbf{r}) \left[ \xi_H^{(v)}(\mathbf{r}) + \int_{\mathcal{H}} \mathcal{G}_B(\mathbf{r}, \mathbf{r}') J_{\Delta}^{(v)}(\mathbf{r}') d\mathbf{r}' \right] + \tau_H(\mathbf{r}) \int_{\mathcal{H}} \mathcal{G}_B(\mathbf{r}, \mathbf{r}') J_{\Delta}^{(v)}(\mathbf{r}') d\mathbf{r}'. \quad (8)$$

By introducing the auxiliary parameter  $\beta(\mathbf{r})$  [25] and defining the modified contrast function  $\chi$  [ $\chi(\mathbf{r}) \triangleq \frac{\beta(\mathbf{r})\tau(\mathbf{r})}{\beta(\mathbf{r})\tau(\mathbf{r})+1}$ ], (8) is then rewritten in the co-called Differential *CIE* (*DCIE*) form [56]

$$\begin{aligned} \beta(\mathbf{r}) J_{\Delta}^{(v)}(\mathbf{r}) = & \chi_{\Delta}(\mathbf{r}) \left[ \xi_H^{(v)}(\mathbf{r}) + \int_{\mathcal{H}} \mathcal{G}_B(\mathbf{r}, \mathbf{r}') J_{\Delta}^{(v)}(\mathbf{r}') d\mathbf{r}' + \beta(\mathbf{r}) J_{\Delta}^{(v)}(\mathbf{r}') + \beta(\mathbf{r}) J_H^{(v)}(\mathbf{r}) \right] \\ & + \chi_H(\mathbf{r}) \left[ \int_{\mathcal{H}} \mathcal{G}_B(\mathbf{r}, \mathbf{r}') J_{\Delta}^{(v)}(\mathbf{r}') d\mathbf{r}' + \beta(\mathbf{r}) J_{\Delta}^{(v)}(\mathbf{r}') \right] \end{aligned} \quad (9)$$

where  $\chi_H$  [ $\chi_H(\mathbf{r}) \triangleq \frac{\beta(\mathbf{r})\tau_H(\mathbf{r})}{\beta(\mathbf{r})\tau_H(\mathbf{r})+1}$ ] and  $\chi_{\Delta}$  [ $\chi_{\Delta}(\mathbf{r}) \triangleq \chi(\mathbf{r}) - \chi_H(\mathbf{r})$ ] are the host-medium and the differential modified contrast, respectively.

Within the above *DCIE* formulation, the solution of the original *ISP* is then recast to that of determining the distribution of the differential modified contrast  $\chi_{\Delta}$  (i.e., the *primary* unknown) and the  $V$  differential equivalent currents,  $\{J_{\Delta}^{(v)}; v = 1, \dots, V\}$  (i.e., the *secondary* unknowns), that fulfil (7) and (9).

Towards this end, (7)(9) are first discretized by partitioning the investigation domain  $\mathcal{H}$  into  $N$  square sub-units,  $\{\mathcal{H}_n; n = 1, \dots, N\}$  ( $\mathcal{H} = \sum_{n=1}^N \mathcal{H}_n$ ), centered at  $\{\mathbf{r}_n; n = 1, \dots, N\}$  and using  $M(N)$  Dirac's test functions to sample (7)(9) at the  $M(N)$  locations of the probes in the observation(investigation) domain  $\{\mathbf{r}_m; m = 1, \dots, M\}(\{\mathbf{r}_m; n = 1, \dots, N\})$ . The following numerical forms of (7)(9) are then derived

$$\bar{\xi}_{sca,\Delta}^{(v)} = \bar{\mathcal{G}}_{\text{ext}} \bar{J}_{\Delta}^{(v)} \quad (10)$$

$$\begin{aligned} \bar{\beta} \otimes \bar{J}_{\Delta}^{(v)} = & \bar{\chi}_{\Delta} \otimes \left[ \bar{\xi}_H^{(v)} + \bar{\mathcal{G}}_{\text{int}} \bar{J}_{\Delta}^{(v)} + \bar{\beta} \otimes \bar{J}_{\Delta}^{(v)} + \bar{\beta} \otimes \bar{J}_H^{(v)} \right] \\ & + \bar{\chi}_H \otimes \left[ \bar{\mathcal{G}}_{\text{int}} \bar{J}_{\Delta}^{(v)} + \bar{\beta} \otimes \bar{J}_{\Delta}^{(v)} \right], \end{aligned} \quad (11)$$

where  $\bar{\xi}_{sca,\Delta}^{(v)} = \{\xi_{sca,\Delta}^{(v)}(\mathbf{r}_m); m = 1, \dots, M\}$ ,  $\bar{\beta} = \{\beta(\mathbf{r}_n); n = 1, \dots, N\}$ ,  $\bar{J}_{\Delta}^{(v)} = \{J_{\Delta}^{(v)}(\mathbf{r}_n); n = 1, \dots, N\}$ ,  $\bar{\chi}_{\Delta} = \{\chi_{\Delta}(\mathbf{r}_n); n = 1, \dots, N\}$ ,  $\bar{\xi}_H^{(v)} = \{\xi_H^{(v)}(\mathbf{r}_n); n = 1, \dots, N\}$ , and  $\bar{J}_H^{(v)} = \{J_H^{(v)}(\mathbf{r}_n); n = 1, \dots, N\}$ , while  $\otimes$  stands for the element-wise multiplication. Moreover,  $\bar{\mathcal{G}}_{\text{int}}(\bar{\mathcal{G}}_{\text{ext}})$  is the  $N \times N(M \times N)$  internal(external) Green's matrix whose  $(p, q)$ -th [ $(m, n)$ -th] ( $p, q = 1, \dots, N$ ) ( $m = 1, \dots, M; n = 1, \dots, N$ ) entry is given by  $\mathcal{G}_{\text{int}}^{pq} = j \frac{k_B^2}{4} \int_{\mathcal{H}_q} H_0^{(2)}(k_B |\mathbf{r}_p - \mathbf{r}'|) d\mathbf{r}' (\mathcal{G}_{\text{ext}}^{mn} = j \frac{k_B^2}{4} \int_{\mathcal{H}_n} H_0^{(2)}(k_B |\mathbf{r}_m - \mathbf{r}'|) d\mathbf{r}')$ ,  $k_B$  being the wavenumber ( $k_B \triangleq \frac{2\pi}{\lambda_B}$ ), while  $H_0^{(2)}(\cdot)$  is the 0-th order Hankel function of the second kind.

### 3 *ISP Solution (MS-DCIE Inversion Method)*

The solution of the inverse problem formulated in Sect. 2 (i.e., the estimation of the spatial distribution within  $\mathcal{H}$  of both the differential modified contrast,  $\bar{\chi}_\Delta$ , and the differential equivalent currents,  $\{\bar{J}_\Delta^{(v)}; v = 1, \dots, V\}$ ) is addressed with an approach based on the application of the *MS* scheme to the *DCIE* formulation of the *ISP*. More specifically, the scattering-data inversion is carried out by means of an iterative strategy that performs  $S$  successive “zooming” steps. At each  $s$ -th ( $s = 1, \dots, S$ ;  $s$  being the step index) step, the spatial distribution of the generic unknown  $\bar{\varphi}$  ( $\bar{\varphi} \in \{\bar{\chi}_\Delta, (\bar{J}_\Delta^{(v)}; v = 1, \dots, V)\}$ ) in the corresponding *RoI*,  $\mathcal{S}_\varphi$ , which is the portion of the investigation domain  $\mathcal{H}$  where  $\varphi(\mathbf{r}_n) \neq 0$ , is retrieved by means of an inversion algorithm as applied to (10) and (11). Such a reconstruction is then exploited to improve the *RoI* estimate by also enhancing the spatial resolution of the retrieval. The process is repeated until a data-matching convergence criterion holds true.

The implementation of such a multi-level process needs: (a) to define the *RoI* for both the primary,  $\mathcal{S}_{\Delta\chi}$ , and the secondary,  $\mathcal{S}_{\Delta J}$ , unknowns (Sect. “*RoI Definition*”); (b) to choose an inversion method to process, at each  $s$ -step ( $s = 1, \dots, S$ ), the scattering data for determining the spatial distribution of the generic unknown  $\bar{\varphi}$  in the corresponding *RoI*,  $\mathcal{S}_\varphi^{(s)}$  (Sect. “*SOM Inversion*”); (c) to define a suitable cost function that faithfully links the *ISP* at hand with its mathematical formulation within the *DCIE* framework so that the actual *ISP* solution coincides with the global minimum of the cost function itself (Sect. “*Cost Function Definition*”); (d) to customize the meta-level *MS* strategy to both such a formulation (i.e., problem unknowns and cost function) and the integration with the optimization level (Sect. “*MS Implementation*”). These items will be detailed or briefly recalled in the following.

#### ***RoI Definition***

To properly address this issue, let us first recall the case of the *MS* as applied to the *CIE* formulation for the *ISP* with homogeneous media. There, the *CIE* unknowns are the modified contrast function,  $\chi$ , and the  $V$  equivalent currents,  $\{\bar{J}^{(v)}; v = 1, \dots, V\}$ , whose supports, namely  $\mathcal{S}_\chi$  and  $\mathcal{S}_J$ , coincide with the extension  $\mathcal{S}_{\Delta\tau}$  of the unknown object  $\mathcal{O}$ , which is modeled by  $\tau_\Delta$  ( $\mathcal{S}_\chi = \mathcal{S}_J \equiv \mathcal{S}_{\Delta\tau}$ ). Therefore, the *RoIs* of both the primary unknown and the secondary one,



which are identified at each  $s$ -th ( $s = 1, \dots, S$ ) *MS* step (i.e.,  $\mathcal{S}_\chi^{(s)}$  and  $\mathcal{S}_J^{(s)}$ ), are the same region where the unknown object is most likely to be present [59] (i.e.,  $\mathcal{S}_\chi^{(s)} = \mathcal{S}_J^{(s)} \equiv \mathcal{S}_{\Delta\tau}^{(s)}$ ).

Otherwise, the problem unknowns for the *DCIE* formulation are the differential modified contrast,  $\chi_\Delta$ , and the  $V$  differential equivalent currents,  $\{\bar{\mathcal{J}}_\Delta^{(v)}; v = 1, \dots, V\}$ ,  $\mathcal{S}_{\Delta\chi}$  and  $\mathcal{S}_{\Delta J}$  being the corresponding supports, respectively. While  $\mathcal{S}_{\Delta\chi}$  is equal to the area occupied by the unknown scatterer and the standard *RoI* definition applies ( $\mathcal{S}_{\Delta\chi} \equiv \mathcal{S}_{\Delta\tau}$ ),  $\mathcal{S}_{\Delta J}$  might also span outside the object region  $\mathcal{O}$  (i.e.,  $\mathcal{S}_{\Delta J} \supseteq \mathcal{S}_{\Delta\tau}$ ) since the equivalent currents,  $\{\bar{\mathcal{J}}_\Delta^{(v)}; v = 1, \dots, V\}$ , as well as the differential ones,  $\{\bar{\mathcal{J}}_\Delta^{(v)}; v = 1, \dots, V\}$ , are here induced also in the external inhomogeneous host medium. As detailed in Appendix B, the *RoI* of  $\bar{\mathcal{J}}_\Delta^{(v)}$  at the  $s$ -th ( $s = 1, \dots, S$ ) *MS* step turns out to be

$$\mathcal{S}_{\Delta J}^{(s)} = \mathcal{S}_{\Delta\chi}^{(s)} \cup \mathcal{S}_{\chi_H}. \quad (12)$$

### **SOM Inversion**

Concerning the inversion method, the *SOM* [2] is adopted for the following reasons. First, the scattering operator  $\bar{\bar{\mathcal{G}}}_{\text{ext}}$  in (10) is compact, thus the *ISP* at hand is ill-posed [10]. In particular, the *ISP* is not unique because of the (possible) presence of non-radiating components of the induced equivalent currents, which do not contribute to the scattered field  $\xi_{sca,\Delta}^{(v)}$  collected in the observation domain external to  $\mathcal{H}$ . To recover uniqueness, it is then necessary to take into account these components during the inversion process as the *SOM* does. Second, thanks to the properties of the *DCIE* formulation, the *ISP* nonlinearity is mitigated, thus the use of a deterministic fast inversion method, instead of computationally-demanding “bare” global optimization techniques [65], could be profitable.

According to the guidelines in [12], the *SOM* is customized to the *DCIE* formulation, towards the integration within the *MS* processing scheme, as follows. The  $v$ -th ( $v = 1, \dots, V$ ) differential equivalent current  $\bar{\mathcal{J}}_\Delta^{(v)}$  is decomposed in two parts, namely the deterministic component,  $\bar{\mathcal{J}}_{\Delta,DP}^{(v)}$ , and the ambiguous one,  $\bar{\mathcal{J}}_{\Delta,AP}^{(v)}$ , which includes the non-radiating terms

$$\bar{\mathcal{J}}_\Delta^{(v)} = \bar{\mathcal{J}}_{\Delta,DP}^{(v)} + \bar{\mathcal{J}}_{\Delta,AP}^{(v)}. \quad (13)$$

The former,  $\bar{\mathcal{J}}_{\Delta,DP}^{(v)}$  ( $v = 1, \dots, V$ ), is computed from (10) by applying the singular value de-

composition (SVD) to the external Green's matrix  $\overline{\overline{G}}_{ext}$ . It turns out that

$$\overline{J}_{\Delta,DP}^{(v)} = \sum_{n=1}^{N_{th}} \frac{(\overline{U}_n)^* \cdot \overline{\xi}_{sca,\Delta}^{(v)}}{\sigma_n} \overline{W}_n \quad (14)$$

where  $*$  stands for conjugate transposition, while  $\cdot$  denotes the scalar product. Moreover,  $\{\sigma_n; n = 1, \dots, N\}$  are the  $N$  singular values of  $\overline{\overline{G}}_{ext}$ , while  $\{\overline{U}_n; n = 1, \dots, N\}$  and  $\{\overline{W}_n; n = 1, \dots, N\}$  are the  $M$ -size left-singular vectors and the  $N$ -size right-singular vectors, respectively. In (14),  $N_{th}$  is the SVD truncation threshold, which is adaptively set as follows [58]

$$N_{th} = \arg \min_{N'} \left\{ \left| \frac{\sum_{n=1}^{N'} \sigma_n}{\sum_{n=1}^N \sigma_n} - \alpha \right| \right\}, \quad (15)$$

$\alpha$  ( $0 < \alpha \leq 1$ ) being a real user-defined calibration parameter as detailed in Sect. 4.

The ambiguous current component,  $\overline{J}_{\Delta,AP}^{(v)}$  ( $v = 1, \dots, V$ ), is related to the smaller singular values of  $\overline{\overline{G}}_{ext}$  and it is yielded by the linear combination of the remaining  $(N - N_{th})$  right-singular vectors

$$\overline{J}_{\Delta,AP}^{(v)} = \sum_{n=N_{th}+1}^N c_{n-N_{th}}^{(v)} \overline{W}_n \quad (16)$$

where  $\overline{c}^{(v)} = \{c_n^{(v)}; n = 1, \dots, (N - N_{th})\}$  is the unknown complex algebraic vector of the weights of the  $v$ -th ( $v = 1, \dots, V$ ) ambiguous current, while  $\overline{c}$  is the corresponding  $(N - N_{th}) \times V$  size matrix ( $\overline{c} \triangleq \{\overline{c}^{(v)}; v = 1, \dots, V\}$ ).

### Cost Function Definition

The cost function  $\Psi$  quantifies the error in fulfilling (10) and (11) and it is defined as

$$\Psi(\overline{c}, \overline{\chi}_\Delta) = \sum_{v=1}^V \left[ \frac{\Psi_{data}^{(v)}(\overline{c}^{(v)})}{\|\overline{\xi}_{sca,\Delta}^{(v)}\|^2} + \frac{\Psi_{state}^{(v)}(\overline{c}^{(v)}, \overline{\chi}_\Delta)}{\|\overline{\xi}_{inc}^{(v)}\|^2} \right] \quad (17)$$

where  $\|\cdot\|$  is the  $\ell_2$ -norm, while the data equation mismatch,  $\Psi_{data}^{(v)}$ , is derived from (10)

$$\Psi_{data}^{(v)}(\overline{c}^{(v)}) = \left\| \overline{\overline{G}}_{ext} \left[ \overline{J}_{\Delta,DP}^{(v)} + \sum_{n=N_{th}+1}^N c_{n-N_{th}}^{(v)} \overline{W}_n \right] - \overline{\xi}_{sca,\Delta}^{(v)} \right\|^2, \quad (18)$$

and the state equation mismatch  $\Psi_{\text{state}}^{(v)}$  stems from (11)

$$\Psi_{\text{state}}^{(v)}(\bar{c}^{(v)}, \bar{\chi}_\Delta) \triangleq \left\| \Psi_{AP}^{(v)}(\bar{c}^{(v)}, \bar{\chi}_\Delta) - \Psi_{DP}^{(v)}(\bar{\chi}_\Delta) \right\|^2, \quad (19)$$

$\Psi_{AP}^{(v)}$  and  $\Psi_{DP}^{(v)}$  being the terms dependent on the *AP* and the *DP* components, respectively, whose expressions are

$$\begin{aligned} \Psi_{AP}^{(v)}(\bar{c}^{(v)}, \bar{\chi}_\Delta) \triangleq & \bar{\beta} \otimes \bar{J}_{\Delta, AP}^{(v)}(\bar{c}^{(v)}) \\ & - (\bar{\chi}_\Delta + \bar{\chi}_H) \otimes \bar{\mathcal{G}}_{\text{int}} \bar{J}_{\Delta, AP}^{(v)}(\bar{c}^{(v)}) \\ & - (\bar{\chi}_\Delta + \bar{\chi}_H) \otimes \bar{\beta} \otimes \bar{J}_{\Delta, AP}^{(v)}(\bar{c}^{(v)}) \end{aligned} \quad (20)$$

and

$$\begin{aligned} \Psi_{DP}^{(v)}(\bar{\chi}_\Delta) \triangleq & -\bar{\beta} \otimes \bar{J}_{\Delta, DP}^{(v)} + \bar{\chi}_\Delta \otimes \left( \bar{\xi}_H^{(v)} + \bar{\beta} \otimes \bar{J}_H^{(v)} \right) \\ & + (\bar{\chi}_\Delta + \bar{\chi}_H) \otimes \left( \bar{\mathcal{G}}_{\text{int}} \bar{J}_{\Delta, DP}^{(v)} + \bar{\beta} \otimes \bar{J}_{\Delta, DP}^{(v)} \right). \end{aligned} \quad (21)$$

## MS Implementation

Within the *DCIE* framework, the algorithmic implementation of the *MS* scheme as integrated into the *SOM*-based inversion can be described through the following multi-step iterative ( $i$  being the iteration index) process:

- *Initialization* - Initialize the *MS* step index ( $s = 1$ ) and the *RoI* for both the unknowns to the whole investigation domain [ $\mathcal{S}_{\Delta\chi}^{(1)} = \mathcal{S}_{\Delta J}^{(1)} = \mathcal{H}$  - Fig. 2(a)];
- *MS Loop*
  - *Unknowns Setup* ( $i = 0$ ) - If  $s = 1$ , then reset the unknowns (i.e.,  $[\bar{\chi}_\Delta^{(s)}]_i = \bar{0}$  and  $[\bar{c}^{(s)}]_i = \bar{0}$ ). Otherwise (i.e.,  $s > 1$ ), map the trial solution from the previous zooming step into the current  $s$ -th discretization grids of the *RoIs*  $\{\mathcal{S}_\varphi^{(s)}; \varphi \in \{\Delta\chi, \Delta J\}\}$  (i.e.,  $[\bar{\chi}_\Delta^{(s)}]_i = \Phi_{\Delta\chi} \left\{ [\bar{\chi}_\Delta^{(s-1)}]_i; \mathcal{S}_{\Delta\chi}^{(s)} \right\}$  and  $[\bar{J}_\Delta^{(v)}]_i^{(s)} = \Phi_{\Delta J} \left\{ [\bar{J}_\Delta^{(v)}]_i^{(s-1)}; \mathcal{S}_{\Delta J}^{(s)} \right\}$ ,  $[\bar{J}_\Delta^{(v)}]_i^{(s-1)}$  being equal to  $[\bar{J}_\Delta^{(v)}]_i^{(s-1)} = \bar{J}_{\Delta, DP}^{(v)} + \sum_{n=N_{th}+1}^N [c_{n-N_{th}}^{(v)}]_i^{(s-1)} \bar{W}_n$ ),  $\Phi_\varphi$  being the mapping operator from the grid of  $\mathcal{S}_\varphi^{(s-1)}$  to the finer one of  $\mathcal{S}_\varphi^{(s)}$ ;
  - *Scattering-Data Inversion* - Compute the *DCIE* regularization parameter vector  $\bar{\beta}^{(s)}$

=  $\{\beta(\mathbf{r}_n); n = 1, \dots, N\}$  by setting its  $N$  entries to the value

$$\beta^{(s)} = \gamma \times \max_{\mathbf{r}_n \in \mathcal{S}_{\Delta J}^{(s)}} \left| \int_{\mathcal{S}_{\Delta J}^{(s)}} \mathcal{G}_{\text{int}}(\mathbf{r}_n, \mathbf{r}') d\mathbf{r}' \right| \quad (22)$$

where  $\gamma$  is a control parameter [25]. Retrieve the  $s$ -th step set of unknowns ( $\bar{\chi}_{\Delta}^{(s)}$ ,  $\bar{c}^{(s)}$ ) within the corresponding  $RoI \mathcal{S}_{\varphi}^{(s)}$  by solving the following optimization problem

$$\left( \bar{\chi}_{\Delta}^{(s)}, \bar{c}^{(s)} \right) = \arg \min_{\bar{\chi}_{\Delta}, \bar{c}} \{ \Psi(\bar{\chi}_{\Delta}, \bar{c}, ) \} \quad (23)$$

with  $I$  iterations of the deterministic Polak-Ribiere version of the Conjugate Gradient (CG) algorithm [66] (i.e.,  $\bar{\chi}_{\Delta}^{(s)} = [\bar{\chi}_{\Delta}^{(s)}]_{i=I}$ ,  $\bar{c}^{(s)} = [\bar{c}^{(s)}]_{i=I}$ ) starting from  $[\bar{\chi}_{\Delta}^{(s)}]_{i=0}$  and  $[\bar{c}^{(s)}]_{i=0}$ . Update the trial differential current  $[\bar{J}_{\Delta}^{(v)}]^{(s)}$  through (13) by using (14) and (16) with  $c_{n-N_{th}}^{(v)} \leftarrow [c_{n-N_{th}}^{(v)}]^{(s)}$ ;

- *Step Check* - Halt the *MS* loop if the maximum number of zooming steps is reached [i.e.,  $s = S$  - Fig. 2(d)], define the estimated solution by setting  $\bar{\chi}_{\Delta}^{opt} = \bar{\chi}_{\Delta}^{(S)}$  and  $[\bar{J}_{\Delta}^{(v)}]^{opt} = [\bar{J}_{\Delta}^{(v)}]^{(S)}$  as well as  $\beta^{opt} = \beta^{(S)}$ , and go to the “*Termination*”;
- *RoI Update* - Apply the “filtering and clustering” operations [51] on  $\bar{\chi}_{\Delta}^{(s)}$  to determine the corresponding new *RoI*,  $\mathcal{S}_{\Delta \chi}^{(s+1)}$  [Figs. 2(b)-2(c)], by defining its center,  $\mathbf{r}_{\Delta \chi}^{(s+1)}$  [ $\mathbf{r}_{\Delta \chi}^{(s+1)} = (x_{\Delta \chi}^{(s+1)}, y_{\Delta \chi}^{(s+1)})$ ], and side,  $L_{\Delta \chi}^{(s+1)}$ , as follows

$$\varsigma_{\Delta \chi}^{(s+1)} = \frac{\sum_{n=1}^N \varsigma_n^{(s)} \chi_{\Delta}^{(s)}(\mathbf{r}_n)}{\sum_{n=1}^N \chi_{\Delta}^{(s)}(\mathbf{r}_n)} \quad (24)$$

( $\varsigma \in \{x; y\}$ ) and

$$L_{\Delta \chi}^{(s+1)} = 2 \times \frac{\sum_{n=1}^N \left\| \mathbf{r}_n^{(s)} - \mathbf{r}_{\Delta \chi}^{(s+1)} \right\| \chi_{\Delta}^{(s)}(\mathbf{r}_n)}{\sum_{n=1}^N \chi_{\Delta}^{(s)}(\mathbf{r}_n)}. \quad (25)$$

Identify the new *RoI* for  $[\bar{J}_{\Delta}^{(v)}]$  (i.e.,  $\mathcal{S}_{\Delta J}^{(s+1)}$ ) through (12);

- *RoI Check* - Terminate the *MS* loop if the zooming factor  $\eta^{(s)}$ , which is defined as

$$\eta^{(s)} = \frac{|L_{\Delta\chi}^{(s+1)} - L_{\Delta\chi}^{(s)}|}{L_{\Delta\chi}^{(s+1)}}, \quad (26)$$

is below a user-defined threshold  $\eta_{min}$  (i.e.,  $\eta^{(s)} \leq \eta_{min}$ ) and set the problem solution to the current trial one (i.e.,  $\bar{\chi}_{\Delta}^{opt} = \bar{\chi}_{\Delta}^{(s)}$  and  $[\bar{J}_{\Delta}^{(v)}]^{opt} = [\bar{J}_{\Delta}^{(v)}]^{(s)}$  as well as  $\beta^{opt} = \beta^{(s)}$ ). Otherwise, update the *MS* loop index [i.e.,  $s \leftarrow (s + 1)$ ] and restart the “*MS Loop*”;

- *Termination* - Given  $\bar{\chi}_{\Delta}^{opt}$ , compute the modified contrast  $\bar{\chi}^{opt}$  (i.e.,  $\bar{\chi}^{opt} = \bar{\chi}_{\Delta}^{opt} + \bar{\chi}_H$ ) to output the estimated contrast vector  $\bar{\tau}^{opt} = \{\tau^{opt}(\mathbf{r}_n); n = 1, \dots, N\}$  whose  $n$ -th ( $n = 1, \dots, N$ ) entry is equal to

$$\tau^{opt}(\mathbf{r}_n) = \frac{\chi^{opt}(\mathbf{r}_n)}{\beta^{opt} [1 - \chi^{opt}(\mathbf{r}_n)]}. \quad (27)$$

## 4 Numerical and Experimental Results

An extensive set of tests has been carried out to assess the reliability and the performance of the proposed *IS* method. The most representative ones have been selected and reported in the following to (i) provide some general rules for calibrating the control parameters of the *MS-DCIE*, (ii) show the effectiveness of such an implementation of the *MS* scheme to yield high-accuracy reconstructions when dealing with inhomogeneous scenarios, and (iii) provide a comparative analysis with other state-of-the-art approaches.

To quantitatively estimate the accuracy of the reconstructions, let us consider two metrics. The one is a local metric and it is the local error function,  $\mathbb{E}$ , defined as

$$\mathbb{E}(\mathbf{r}) \triangleq \frac{\tau(\mathbf{r}) - \tau^{opt}(\mathbf{r})}{\tau(\mathbf{r}) + 1}, \quad (28)$$

$\tau$  and  $\tau^{opt}$  being the actual and the reconstructed contrast, respectively. The other metric gives

a global/integral information on the imaging process and it is given by

$$\Xi \triangleq \frac{1}{\mathcal{A}} \sum_{r_n \in \mathcal{A}} |\mathbb{E}(\mathbf{r}_n)|, \quad (29)$$

where  $\mathcal{A}$  is the area of the region where the error figure is evaluated. More specifically,  $\Xi = \Xi_{tot}$ ,  $\Xi = \Xi_{int}$ , and  $\Xi = \Xi_{ext}$  if  $\mathcal{A} = \mathcal{H}$ ,  $\mathcal{A} = \mathcal{S}_{\Delta\tau}$ , and  $\{\mathcal{H} \setminus \mathcal{S}_{\Delta\tau}\}$ , respectively.

Unless otherwise stated, the side of the square investigation domain  $\mathcal{H}$  has been set to  $L_{\mathcal{H}} = 3 \times \lambda_B$ ,  $\lambda_B$  being the wavelength in the external background. Such a benchmark scenario has been probed by  $V = 27$  directions, while the scattering data have been collected in  $M = 27$  uniformly-spaced locations on a circle of radius  $\rho = 2.2 \times \lambda_B$  and centered in the host medium region  $\mathcal{H}$ . In all numerical tests, the scattered field samples in (10) have been synthetically-generated by solving the forward (*FW*) scattering problem with a Method of Moments (*MoM*) solver and discretizing the investigation domain with  $N_{FW} = 80 \times 80$  square cells. Moreover, the data samples have been blurred with an additive Gaussian noise, characterized by a signal-to-noise ratio (*SNR*), to model realistic measurement conditions. As for the data inversion, a coarser discretization grid has been assumed (i.e.,  $N = 30 \times 30$ ) to represent the contrast profile at each  $s$ -th ( $s = 1, \dots, S$ ) *MS* step. The maximum number of *MS* steps has been set to  $S = 6$ , while  $I = 200$  *SOM* iterations have been executed at each  $s$ -th *MS* step according to the guidelines in [59]. Lastly, the value of  $\eta_{min} = 0.2$  has been selected for the *MS* zooming threshold according to [64].

#### 4.1 Parameters Calibration and Sensitivity Analysis

The behavior of the *MS-DCIE* inversion method mainly depends on the values of two control parameters:  $\alpha$ , which determines the *SVD* truncation threshold  $N_{th}$ , and  $\gamma$ , which controls the *DCIE* regularization at each *MS* step. To determine their optimal trade-off setup, a sensitivity analysis has been performed and the representative results from the benchmark scenario in Fig. 1 are reported hereinafter for illustration purposes. More in detail, an off-centered square scatterer  $0.7\lambda_B$ -sided with unknown differential contrast  $\tau_{\Delta} = 2$  [Fig. 1(c)], located at  $(x_O, y_O) = (0.3 \lambda_B, 0.15 \lambda_B)$  [Fig. 1(b)], and surrounded by a known host domain composed

by a centered square ring of thickness  $0.3\lambda_B$  with  $\tau_H^{(1)} = 0.5$  [Fig. 1(b)] and a remaining area of contrast  $\tau_H^{(2)} = 0.0$ , has been retrieved by applying the *MS-DCIE* strategy with different values of the control parameters and for different *SNRs*.

The analysis outcomes are summarized in Fig. 3 where the behavior of the total reconstruction error  $\Xi_{tot}$  versus  $\alpha$  [Fig. 3(a)] and  $\gamma$  [Fig. 3(b)] is shown in correspondence with different noise level on the scattering data. It turns out that the  $\alpha$  value has a low impact on the *MS-DCIE* performance,  $\Xi_{tot}$  being almost flat or with a limited range of variations for a given value of *SNR*. On the contrary, the  $\gamma$  parameter has a more notable effect on the reconstruction accuracy since it “controls” the non-linearity of the inverse problem at hand [25]. The optimal setup for  $\alpha$  and  $\gamma$  has then been chosen according to the following rule

$$\zeta^* = \frac{\int_{SNR} \arg \min_{\zeta} \left\{ \Xi_{tot} \Big|_{SNR}^{\zeta} \right\} dSNR}{\int_{SNR} dSNR} \quad (30)$$

( $\zeta = \{\alpha; \gamma\}$ ) and the result has been  $(\alpha^*, \gamma^*) = (0.4, 1.4)$ .

## 4.2 Numerical Assessment

Once calibrated, the performance of the *MS-DCIE* have been assessed in comparison with competitive state-of-the-art inversion approaches. First, the comparison with the single-resolution *DCIE*<sup>(1)</sup> has been carried out. The test case refers to the “Square” scatterer in Sect. 4.1 and the scattering data have been blurred with  $SNR = 20$  [dB]. Figure 4 shows the evolution of the cost function,  $\Psi$ , the total error,  $\Xi_{tot}$ , and the *MS* zooming factor,  $\eta^{(s)}$ , during the *MS* process. Moreover, the color-maps of the retrieved differential contrast,  $\tau_{\Delta}$ , are reported in Fig. 5, as well. As it can be observed, the estimated  $\mathcal{S}_{\Delta\tau}$ -*RoI* shrinks around the actual object position [Figs. 5(a)-5(c)] until there is an almost perfect match with the scatterer support [Fig. 5(d)]. This occurs at  $s = 4$  when the value of  $\eta^{(s)}$  falls below the threshold  $\eta_{min}$  (Fig. 4) and the inversion process is stopped. It is worth noticing that during the *MS* procedure both the cost function and the reconstruction error decrease (Fig. 4) by pointing out the enhancement of the inversion

---

<sup>(1)</sup>According to the guidelines in [25], the regularization parameter has been set to  $\beta = 2$ , while the investigation domain  $\mathcal{H}$  has been partitioned in  $N_{DCIE} = 46 \times 46$  square cells.

accuracy in correspondence with a better fitting with the scattering data. The contrast profile  $\tau^{opt}$  derived by the *MS-DCIE* [Fig. 5(e)] is then compared with that retrieved with the *DCIE* method [Fig. 5(f)]. Both pictorially and quantitatively, it is evident that the *MS*-based inversion significantly improves the reconstruction inside(outside) the object support. Indeed, the internal/external error reduces of about  $\Theta\Xi_{int} = 77\%$  ( $\Theta\Xi_{ext} = 52\%$ ) ( $\Theta\Xi \triangleq \frac{\Xi^{DCIE} - \Xi^{MS-DCIE}}{\Xi^{DCIE}}$ ) with respect to the single-resolution approach.

The comparative assessment has been extended next to the strategies based on the *DLSIE* formulation [56][59], which are referred in the following as *MS-DLSIE* and *DLSIE*, respectively, and the results from the analysis on scenario ‘‘Circular-Ring’’ object, shown in the inset of Fig. 6, are reported hereinafter. Figure 6 plots the values of  $\Xi_{tot}$  versus the *SNR* for the different inversion methods. One can observe that the *DCIE* formulation turns out to be better than the *DLSIE* one as visually confirmed by the error maps at *SNR* = 20 [dB] reported in Fig. 7 [e.g., Fig. 7(a) vs. Fig. 7(c) and Fig. 7(b) vs. Fig. 7(d)]. Moreover, as expected, the multi-resolution implementations yield better reconstructions with lower errors than their single-resolution counterparts for any *SNR* (Fig. 6 -  $\Xi_{tot}^{MS-DCIE} < \Xi_{tot}^{DCIE}$  and  $\Xi_{tot}^{MS-DLSIE} < \Xi_{tot}^{DLSIE}$ ) by reducing the artifacts at the scatterer edges and outside the object within the host medium [e.g., Fig. 7(a) vs. Fig. 7(b) and Fig. 7(c) vs. Fig. 7(d)].

The performance of the *MS-DCIE* have been assessed also against the scatterer permittivity, thus verifying its accuracy against a higher non-linearity of the *ISP*. Towards this end, the actual contrast of the circular ring object has been varied in the range from  $\tau_{\Delta} = 2$  up to  $\tau_{\Delta} = 4$ , while keeping the noise level to *SNR* = 20 [dB]. The plots of the reconstruction indexes in Fig. 8 point out that the inversion becomes more and more difficult when the differential contrast becomes stronger and stronger since all errors get larger, but they also point out the effectiveness of the *MS* in dealing with stronger scatterers with an average improvement of the total(external) error,  $\Xi_{tot}(\Xi_{ext})$ , of about 45 % (48 %) with respect to the *DCIE* single-resolution strategy. Moreover, the higher the contrast is the greater is the advantage of using the *MS* for imaging the unknown object support since the internal error gap  $\Theta\Xi_{int}$  grows as  $\tau_{\Delta}$  tends to  $\tau_{\Delta} = 4$  (i.e.,  $\Theta\Xi_{int}|_{\tau_{\Delta}=2} = 12\%$ ,  $\Theta\Xi_{int}|_{\tau_{\Delta}=3} = 37\%$ , and  $\Theta\Xi_{int}|_{\tau_{\Delta}=4} = 51\%$ ). These outcomes are highlighted by the error maps related to  $\tau_{\Delta} = 2$  [Figs. 7(a)-7(b)],  $\tau_{\Delta} = 3$  [Fig. 9(a) and Fig.



9(c)], and  $\tau_\Delta = 4$  [Fig. 9(b) and Fig. 9(d)].

Another numerical experiment has been devoted to assess the *MS-DCIE* when dealing with lossy scatterers (i.e.,  $\sigma_\Delta \neq 0$  [S/m]). By keeping the ring target of Fig. 6, its differential contrast has been set to  $\text{Re}\{\tau_\Delta\} = 2$ , while the actual scatterer conductivity has been varied within the range  $10^{-3}$  [S/m]  $\leq \sigma_\Delta \leq 1$  [S/m] ( $f = 300$  [MHz]). Unlike the dependence on the scatterer permittivity in Fig. 8, the accuracy improvement of the *MS* strategy reduces as the object conductivity increases (e.g.,  $\Theta_{\Xi_{tot}}|_{\sigma_\Delta=10^{-3}$  [S/m]} = 56 %,  $\Theta_{\Xi_{tot}}|_{\sigma_\Delta=10^{-2}$  [S/m]} = 51 %,  $\Theta_{\Xi_{tot}}|_{\sigma_\Delta=10^{-1}$  [S/m]} = 44 %, and  $\Theta_{\Xi_{tot}}|_{\sigma_\Delta=10^0}$  [S/m]} = 24 % - Fig. 10). However, it is worth noticing that locally the *MS-DCIE* still significantly outperforms the *DCIE* in retrieving the imaginary part of the contrast distribution by better detailing the contours and the support of the unknown circular ring as highlighted by the error maps in Fig. 11 ( $\sigma_\Delta = 10^{-1}$  [S/m]).

The last numerical experiment is aimed at evaluating how an inaccurate knowledge of the host medium contrast,  $\tau_H(\mathbf{r})$ , affects the *MS-DCIE* reconstruction. Towards this end, the *a-priori* information on the host medium has been supposed to be affected by an uncertainty proportional to the constant  $\delta$

$$\hat{\tau}_H(\mathbf{r}) = \tau_H(\mathbf{r}) \times (1 + \delta) \quad (31)$$

and the analysis has been carried out on the ‘‘Square object’’ scenario with  $\tau_\Delta = 2$  and  $SNR = 20$  [dB]. By varying the value of  $\delta$  from 0 % up to 100 %, it is not surprising that all error indexes get worse when the *a-priori* information on the host medium is more and more imprecise (Fig. 12). However, the *MS-DCIE* always yields better reconstructions as quantitatively confirmed by the total error gap  $\Theta_{\Xi_{tot}}$  values (i.e.,  $\Theta_{\Xi_{tot}} \geq 32$  %) even though the improvements with respect to the *DCIE* diminish as the host medium knowledge is getting more inaccurate (i.e.,  $\Theta_{\Xi_{tot}}|_{\delta=0.05} = 71$  % - Fig. 13(a) vs. Fig. 13(b),  $\Theta_{\Xi_{tot}}|_{\delta=0.2} = 60$  % - Fig. 13(c) vs. Fig. 13(d), and  $\Theta_{\Xi_{tot}}|_{\delta=0.8} = 45$  % - Fig. 13(e) vs. Fig. 13(f)).

### 4.3 Experimental Assessment

To complete the validation of the *MS-DCIE* with real data, the results of this section refer to the experimental measurements from the Istitut Fresnel for the ‘‘FoamDieIntTM’’ object [67]. In this test case, the square investigation domain of side  $L_{\mathcal{H}} = 0.4$  [m] has been illuminated

by a ridged-horn antenna from  $V = 8$  different angular directions and the electric-field data samples have been collected by another horn antenna moved in  $M = 241$  uniformly-distributed locations on a circle of radius  $\rho = 1.67$  [m]. Within the investigation domain, there is an inner cylinder with a diameter of  $D_1 = 31$  [mm] and relative permittivity  $\varepsilon_1 = 3$ , which is centered at  $(x_O, y_O) = (-5$  [mm],  $0$  [mm]) and it is surrounded by a larger centered cylinder of diameter  $D_2 = 80$  [mm] having a relative permittivity equal to  $\varepsilon_2 = 1.45$  [Fig. 14(a)].

In order to test the differential formulation of the proposed *IS* method for inhomogeneous media, the outer cylinder has been assumed to be part of the known host medium with contrast  $\tau_H(\mathbf{r})$  [Fig. 14(b)] so that the differential contrast  $\tau_\Delta(\mathbf{r})$  of the inner cylinder is the unknown to be retrieved [Fig. 14(c)]. As for the *a-priori* knowledge on the host medium, it is worthwhile to note that the permittivity of the second/larger cylinder ( $\varepsilon_2 = 1.45$ ) is known with a precision of about  $\pm 0.15$  [67], which corresponds to an uncertainty in (31) of approximately  $\delta = \pm 10\%$ .

For comparison purposes, such real data have been processed with the *IP* methods based on both *DCIE* and *DLSIE* formulations as well as single- and multi-resolution strategies. The data inversion outcomes in terms of the total reconstruction error,  $\Xi_{tot}$ , versus the dataset frequency,  $f$ , are summarized in Tab. I. Generally, *MS*-based implementations yield lower reconstruction errors when compared to their single-step counterparts. The same holds true for the *DCIE* formulation versus the *DLSIE*-based one. Always, the *MS-DCIE* outperforms the other alternative techniques by confirming the conclusions drawn from the numerical analyses in Sect. 4.2.

As for the local accuracy of the reconstructions, let us consider the error maps for some representative cases. For instance, Figures 15-16 show the local error distribution,  $\mathbb{E}(\mathbf{r})$ , yielded when processing the datasets at  $f = 7$  [GHz] (Fig. 15) and  $f = 8$  [GHz] (Fig. 16). As one can observe, the *DLSIE*-based methods fail at correctly estimating the contrast of the unknown scatterer as highlighted by the higher values of the error index in Figs. 15(c)-15(d) and Figs. 16(c)-16(d). On the contrary, the single-resolution *DCIE* reconstructions provide a more reliable estimation of the unknown cylinder permittivity [Fig. 15(b) and Fig. 16(b)], even though the retrieved distributions still present several artifacts outside the scatterer support along with non-negligible errors on the scatterer edges. As expected, the *MS-DCIE* provides the smoothest error distribution in the whole investigation domain [Fig. 15(a) and Fig. 16(a)] and it obtains

a careful representation of the target edges. It is also worthwhile to point out that the average reconstruction error of the *MS-DCIE* within the support of the outer/larger known cylinder is  $\Xi_2]_{f=7[GHz]}^{MR-DCIE} = 14.8 \%$  and  $\Xi_2]_{f=8[GHz]}^{MR-DCIE} = 13.5 \%$ , respectively, those values are very close to the tolerance on the *a-priori* knowledge of the outer cylinder permittivity ( $\delta = \pm 10 \%$ ). Such results further assess the remarkable reconstruction capabilities of the *MS-DCIE* despite the approximate knowledge of the inhomogeneous host medium.

## 5 Conclusions

A novel inversion method, named *MS-DCIE*, has been developed to address the *ISPs* with inhomogeneous media. The proposed approach combines the *DCIE* formulation with the *MS* inversion strategy and it has proved to be reliable and effective in a wide range of scenarios and under different conditions. As a matter of fact, the effectiveness of the developed *IS* technique has been tested against both numerical and experimental scattering data by considering lossless and lossy profiles as well as varying the object contrast. The effects of some uncertainty on the *a-priori* knowledge of the host medium have been evaluated, as well.

Future works, beyond the scope of the current manuscript, will be aimed at extending the formulation to three-dimensional (*3D*) geometries as well as at customizing the proposed implementation to biomedical scenarios of great applicative interest.

## Appendix A

With reference to Fig. 1(a) (Scenario “*with object*”) and according to the *LSIE* theory, the *EM* phenomena are described by the “*data equation*”,

$$\xi_{sca}^{(v)}(\mathbf{r}_m) = \int_{\mathcal{H}} \mathcal{G}_B(\mathbf{r}_m, \mathbf{r}') \tau(\mathbf{r}') \xi^{(v)}(\mathbf{r}') d\mathbf{r}', \quad (32)$$

and the “*state equation*”,

$$\xi^{(v)}(\mathbf{r}) = \xi_{inc}^{(v)}(\mathbf{r}) + \int_{\mathcal{H}} \mathcal{G}_B(\mathbf{r}, \mathbf{r}') \tau(\mathbf{r}') \xi^{(v)}(\mathbf{r}') d\mathbf{r}'. \quad (33)$$

Analogously, the *LSIE* equations for the the Scenario “*without the object*” [Fig. 1(a)] turn out

to be

$$\xi_{sca,H}^{(v)}(\mathbf{r}_m) = \int_{\mathcal{H}} \mathcal{G}_B(\mathbf{r}_m, \mathbf{r}') \tau_H(\mathbf{r}') \xi_H^{(v)}(\mathbf{r}') d\mathbf{r}', \quad (34)$$

$$\xi_H^{(v)}(\mathbf{r}) = \xi_{inc}^{(v)}(\mathbf{r}) + \int_{\mathcal{H}} \mathcal{G}_B(\mathbf{r}, \mathbf{r}') \tau_H(\mathbf{r}') \xi_H^{(v)}(\mathbf{r}') d\mathbf{r}'. \quad (35)$$

By subtracting (34) from (32) and (35) from (33), it turns out that

$$\xi_{sca,\Delta}^{(v)}(\mathbf{r}_m) = \int_{\mathcal{H}} \mathcal{G}_B(\mathbf{r}_m, \mathbf{r}') \left[ \tau(\mathbf{r}') \xi^{(v)}(\mathbf{r}') - \tau_H(\mathbf{r}') \xi_H^{(v)}(\mathbf{r}') \right] d\mathbf{r}', \quad (36)$$

$$\xi^{(v)}(\mathbf{r}) = \xi_H^{(v)}(\mathbf{r}) + \int_{\mathcal{H}} \mathcal{G}_B(\mathbf{r}, \mathbf{r}') \left[ \tau(\mathbf{r}') \xi^{(v)}(\mathbf{r}') - \tau_H(\mathbf{r}') \xi_H^{(v)}(\mathbf{r}') \right] d\mathbf{r}'. \quad (37)$$

where  $\xi_{sca,\Delta}^{(v)}$  is the differential scattered field given by the difference between the scattered field with  $\xi_{sca}^{(v)}$  and without  $\xi_{sca,H}^{(v)}$  the unknown object [ $\xi_{sca,\Delta}^{(v)}(\mathbf{r}_m) \triangleq \xi_{sca}^{(v)}(\mathbf{r}_m) - \xi_{sca,H}^{(v)}(\mathbf{r}_m)$ ;  $m = 1, \dots, M$ ;  $v = 1, \dots, V$ ].

Finally, since  $\tau(\mathbf{r}) = \tau_{\Delta}(\mathbf{r}) - \tau_H(\mathbf{r})$  and after simple manipulations, (4) and (5) are yielded.

## Appendix B

The support  $\mathcal{S}_{\varphi}$  of a function  $\varphi$ , referred here as *RoI* of  $\varphi$ , is defined as the region of the investigation domain  $\mathcal{H}$  where the value of the function is non-null

$$\mathcal{S}_{\varphi} \triangleq \{\mathbf{r} : \varphi(\mathbf{r}) \neq 0\}. \quad (38)$$

Since the difference equivalent current,  $J_{\Delta}^{(v)}$ , is given by (6), then its value is non-zero only if either  $J^{(v)}$  or  $J_H^{(v)}$  are non-zero, vice-versa  $J_{\Delta}^{(v)}(\mathbf{r}) = 0$  if  $J^{(v)}(\mathbf{r}) = 0$  and  $J_H^{(v)}(\mathbf{r}) = 0$ . Therefore, the following relation on the support  $\mathcal{S}_{\Delta J}$  of  $J_{\Delta}^{(v)}$  holds true

$$\mathcal{S}_{\Delta J} \subseteq (\mathcal{S}_J \cup \mathcal{S}_{J_H}). \quad (39)$$

Moreover, the  $v$ -th ( $v = 1, \dots, V$ ) equivalent current,  $J^{(v)}(\mathbf{r})$ , is zero if the contrast  $\tau(\mathbf{r})$  is zero being  $J^{(v)}(\mathbf{r}) \triangleq \tau(\mathbf{r}) \xi^{(v)}(\mathbf{r})$ , thus  $\mathcal{S}_J \subseteq \mathcal{S}_{\tau}$ . Analogously,  $\mathcal{S}_{J_H} \subseteq \mathcal{S}_{\tau_H}$  since  $J_H^{(v)}(\mathbf{r}) \triangleq$

$\tau_H(\mathbf{r}) \xi_H^{(v)}(\mathbf{r})$ . Accordingly, (39) can be rewritten as follows

$$\mathcal{S}_{\Delta J} \subseteq (\mathcal{S}_\tau \cup \mathcal{S}_{\tau_H}). \quad (40)$$

Moving to the modified contrasts, given by  $\chi(\mathbf{r}) \triangleq \frac{\beta(\mathbf{r})\tau(\mathbf{r})}{\beta(\mathbf{r})\tau(\mathbf{r})+1}$  and  $\chi_H(\mathbf{r}) \triangleq \frac{\beta(\mathbf{r})\tau_H(\mathbf{r})}{\beta(\mathbf{r})\tau_H(\mathbf{r})+1}$  subject to  $\beta(\mathbf{r}) \neq 0$ , it turns out that  $\mathcal{S}_\chi \equiv \mathcal{S}_\tau$  and  $\mathcal{S}_{\chi_H} \equiv \mathcal{S}_{\tau_H}$ . By combining these latter conclusions with (40), one yields that

$$\mathcal{S}_{\Delta J} \subseteq (\mathcal{S}_\chi \cup \mathcal{S}_{\chi_H}), \quad (41)$$

that assumes the form (12) by observing that  $\mathcal{S}_\chi \equiv (\mathcal{S}_{\Delta\chi} \cup \mathcal{S}_{\chi_H})$  from the definition of  $\chi_\Delta(\mathbf{r})$  [i.e.,  $\chi_\Delta(\mathbf{r}) \triangleq \chi(\mathbf{r}) - \chi_H(\mathbf{r})$ ].

## Acknowledgements

This work benefited from the networking activities carried out within the Project "MITIGO - Mitigazione dei rischi naturali per la sicurezza e la mobilita' nelle aree montane del Mezzogiorno" (Grant no. ARS01\_00964) funded by the Italian Ministry of Education, University, and Research within the PON R&I 2014-2020 Program (CUP: B64I20000450005), the Project "EMvisioning - Cyber-Physical Electromagnetic Vision: Context-Aware Electromagnetic Sensing and Smart Reaction" (Grant no. 2017HZJXSZ) funded by the Italian Ministry of Education, University, and Research within the PRIN2017 Program (CUP: E64I19002530001), and Project "SPEED" (Grant No. 6721001) funded by National Science Foundation of China under the Chang-Jiang Visiting Professorship Program. A. Massa wishes to thank E. Vico for her never-ending inspiration, support, guidance, and help.

## References

- [1] D. Colton and R. Kress, *Inverse Acoustic and Electromagnetic Scattering Theory*. New York, NY, USA: Springer, 2013.
- [2] X. Chen, *Computational Methods for Electromagnetic Inverse Scattering*. Hoboken, NJ, USA: Wiley, 2018.
- [3] T. M. Habashy and A. Abubakar, "A general framework for constraint minimization for the inversion of electromagnetic measurements," *PIER*, vol. 46, pp. 265-312, 2004.
- [4] G. Oliveri, L. Poli, N. Anselmi, M. Salucci, and A. Massa, "Compressive sensing based Born iterative method for tomographic imaging," *IEEE Trans. Microw. Theory Techn.*, vol. 67, no. 5, pp. 1753-1765, May 2019.
- [5] Y. Wang and W. Chew, "An iterative solution of the two-dimensional electromagnetic inverse scattering problem," *J. Imag. Syst. Technol.*, vol. 1, no. 1, pp. 100-108, Jul. 1989.
- [6] W. Zhang, L. Li, and F. Li, "Multifrequency imaging from intensity-only data using the phaseless data distorted Rytov iterative method," *IEEE Trans. Antennas Propag.*, vol. 57, no. 1, pp. 290-295, Jan. 2009.
- [7] W. Chew and Y. Wang, "Reconstruction of two-dimensional permittivity distribution using the distorted Born iterative method," *IEEE Trans. Med. Imag.*, vol. 9, no. 2, pp. 218-225, Jun. 1990.
- [8] R. E. Kleinman and P. M. van den Berg, "A modified gradient method for two-dimensional problems in tomography," *J. Comput. Appl. Math.*, vol. 42, pp. 17-35, 1992.
- [9] R. Kleinman and P. van den Berg, "A contrast source inversion method," *Inverse Probl.*, vol. 13, no. 6, pp. 1607-1620, Jul. 1997.
- [10] O. M. Bucci and T. Isernia, "Electromagnetic inverse scattering: retrievable information and measurement strategies," *Radio Sci.*, vol. 32, no. 6, pp. 2123-2137, 1997.

- [11] P. M. van den Berg, A. Abubakar, and J. Fokkema, "Multiplicative regularization for contrast profile inversion," *Radio Sci.*, vol. 38, no. 2, Apr. 2003.
- [12] X. Chen, "Subspace-based optimization method for solving inverse-scattering problems," *IEEE Trans. Geosci. Remote Sens.*, vol. 48, no. 1, pp. 42-49, Jan. 2010.
- [13] Y. Zhong and X. Chen, "Twofold subspace-based optimization method for solving inverse scattering problems," *Inverse Probl.*, vol. 25, 085003, Jul. 2009.
- [14] A. Franchois and C. Pichot, "Microwave imaging-complex permittivity reconstruction with a Levenberg-Marquardt method," *IEEE Trans. Antennas Propag.*, vol. 45, no. 2, pp. 203-215, Feb. 1997.
- [15] C. Gilmore, P. Mojabi, and J. LoVetri, "Comparison of an enhanced distorted born iterative method and the multiplicative-regularized contrast source inversion method," *IEEE Trans. Antennas Propag.*, vol. 57, no. 8, pp. 2341-2351, Jun. 2009.
- [16] M. Salucci, G. Oliveri, N. Anselmi, F. Viani, A. Fedeli, M. Pastorino, and A. Randazzo, "Three-dimensional electromagnetic imaging of dielectric targets by means of the multi-scaling inexact-Newton method," *J. Opt. Soc. Am. A*, vol. 34, no. 7, pp. 1119-1131, 2017.
- [17] P. Rocca, M. Benedetti, M. Donelli, D. Franceschini, and A. Massa, "Evolutionary optimization as applied to inverse scattering problems," *Inverse Probl.*, vol. 25, no. 12, pp. 123003, Dec. 2009.
- [18] A. Abubakar and P. M. van der Berg, "Total variation as a multiplicative constraint for solving inverse problems," *IEEE Trans. Image Process.*, vol. 10, no. 9, pp. 1384-1392, Jan. 2001.
- [19] K. Xu, Y. Zhong, R. Song, X. Chen, and L. Ran, "Multiplicative-regularized FFT twofold subspace-based optimization method for inverse scattering problems," *IEEE Trans. Geosci. Remote Sens.*, vol. 53, no. 2, pp. 841-850, Jun. 2015.

- [20] G. Oliveri, M. Salucci, N. Anselmi, and A. Massa, "Compressive sensing as applied to inverse problems for imaging: theory, applications, current trends, and open challenges," *IEEE Antennas Propag. Mag.*, vol. 59, no. 5, pp. 34-46, Oct. 2017.
- [21] A. Massa, P. Rocca, and G. Oliveri, "Compressive sensing in electromagnetics - A review," *IEEE Antennas Propag. Mag.*, vol. 57, no. 1, pp. 224-238, Feb. 2015.
- [22] Y. Zhong and X. Chen, "An FFT twofold subspace-based optimization method for solving electromagnetic inverse scattering problems," *IEEE Trans. Antennas Propag.*, vol. 59, no. 3, pp. 914-927, Mar. 2011.
- [23] J. Ma, W. C. Chew, C.-C. Lu, and J. Song, "Image reconstruction from TE scattering data using equation of strong permittivity fluctuation," *IEEE Trans. Antenna Propag.*, vol. 48, no. 6, pp. 860-867, Jun. 2000.
- [24] K. Agarwal, R. Song, M. D'Urso, and X. Chen, "Improving the performances of the contrast source extended Born inversion method by subspace techniques," *IEEE Geosci. Remote Sens. Lett.*, vol. 10, no. 2, pp. 391-395, Aug. 2012.
- [25] Y. Zhong, M. Lambert, D. Lesselier, and X. Chen, "A new integral equation method to solve highly nonlinear inverse scattering problems," *IEEE Trans. Antennas Propag.*, vol. 64, no. 5, pp. 1788-1799, May 2016.
- [26] E. Kilic and T. F. Eibert, "Solution of 3D inverse scattering problems by combined inverse equivalent current and finite element methods," *J. Comput. Phys.*, vol. 288, pp. 131-149, 2015.
- [27] K. G. Brown, N. Geddert, M. Asefi, J. LoVetri, and I. Jeffrey, "Hybridizable discontinuous Galerkin method contrast source inversion of 2-D and 3-D dielectric and magnetic targets," *IEEE Trans. Microw. Theory Techn.*, vol. 67, no. 5, pp. 1766-1777, May 2019.
- [28] T. van Leeuwen and F. J. Herrmann, "A penalty method for PDE- constrained optimization in inverse problems," *Inverse Probl.*, vol. 32, 015007, 2016.



- [29] N. Anselmi, L. Poli, G. Oliveri, and A. Massa, "Iterative multi-resolution Bayesian CS for microwave imaging," *IEEE Trans. Antennas Propag.*, vol. 66, no. 7, pp. 3665-3677, Jul. 2018.
- [30] K. Xu, Y. Zhong, and G. Wang, "A hybrid regularization technique for solving highly nonlinear inverse scattering problems," *IEEE Trans. Microw. Theory Techn.*, vol. 64, no. 5, pp. 11-21, Jan. 2018.
- [31] A. Abubakar and P. M. van den Berg, "Three-dimensional inverse scattering applied to cross-well induction sensors," *IEEE Trans. Antennas Propag.*, vol. 38, no. 4, pp. 1669-1681, Jul. 2000.
- [32] R. Zoughi, *Microwave Nondestructive Testing and Evaluation*. Amsterdam, The Netherlands: Kluwer, 2000.
- [33] A. Abubakar, P. M. van den Berg, and J. Mallorqui, "Imaging of biomedical data using a multiplicative regularized contrast source inversion method," *IEEE Trans. Microw. Theory Techn.*, vol. 50, no. 7, pp. 1761- 1771, Jul. 2002.
- [34] T. Cui, W. C. Chew, A. A. Aydinler, and S. Chen "Inverse scattering of two-dimensional dielectric objects buried in a lossy earth using the distorted Born iterative method," *IEEE Trans. Geosci. Remote Sens.*, vol. 39, no. 2, pp. 339-346, Feb. 2001.
- [35] L. Song, C. Yu, and Q. Liu, "Through-wall imaging (TWI) by radar: 2-D tomographic results and analyses," *IEEE Trans. Antennas Propag.*, vol. 43, no. 12, pp. 2793-2798, Nov. 2005.
- [36] S. Kharkovsky and R. Zoughi, "Microwave and millimeter wave nondestructive testing and evaluation - Overview and recent advances," *IEEE Instrum. Meas. Mag.*, vol. 10, no. 2, pp. 26-38, Apr. 2007.
- [37] M. Zhdanov, *Geophysical inverse theory and regularization problems*. Amsterdam: Elsevier Science, 2007.

- [38] P. Mojabi and J. LoVetri, "Microwave biomedical imaging using the multiplicative regularized Gauss-Newton inversion," *IEEE Antennas Wireless Propag. Lett.*, vol. 8, pp. 645-648, Jul. 2009.
- [39] M. Salucci, G. Oliveri, and A. Massa, "GPR prospecting through an inverse scattering frequency-hopping multi-focusing approach," *IEEE Trans. Geosci. Remote Sens.*, vol. 53, no. 12, pp. 6573-6592, Dec. 2015.
- [40] M. Fallahpour and R. Zoughi, "Fast 3-D qualitative method for through-wall imaging and structural health monitoring," *IEEE Geosci. Remote Sens. Lett.*, vol. 12, no. 12, pp. 2463-2467, Dec. 2015.
- [41] M. Salucci, N. Anselmi, G. Oliveri, P. Calmon, R. Miorelli, C. Reboud, and A. Massa, "Real-time *NDT-NDE* through an innovative adaptive partial least squares *SVR* inversion approach," *IEEE Trans. Geosci. Remote Sens.*, vol. 54, no. 11, pp. 6818-6832, Nov. 2016.
- [42] Z. Wei, Y. Cui, E. Ma, S. Johnston, Y. Yang, R. Chen, M. Kelly, Z. Shen, and X. Chen, "Quantitative theory for probe-sample interaction with inhomogeneous perturbation in near-field scanning microwave microscopy," *IEEE Trans. Microw. Theory Techn.*, vol. 64, no. 5, pp. 1402-1408, May 2016.
- [43] M. Salucci, L. Poli, and A. Massa, "Advanced multi-frequency GPR data processing for non-linear deterministic imaging," *Signal Proc.*, vol. 132, pp. 306-318, Mar. 2017.
- [44] M. Salucci, L. Poli, N. Anselmi, and A. Massa, "Multifrequency particle swarm optimization for enhanced multiresolution GPR microwave imaging," *IEEE Trans. Geosci. Remote Sens.*, vol. 55, no. 3, pp. 1305-1317, Mar. 2017.
- [45] Y. Gao and R. Zoughi, "Millimeter wave reflectometry and imaging for noninvasive diagnosis of skin burn injuries," *IEEE Trans. Instrum. Meas.*, vol. 66, no. 1, pp. 77-84, Jan. 2017.
- [46] Z. Liu, C. Li, D. Lesselier, and Y. Zhong, "Fast full-wave analysis of damaged periodic fiber-reinforced laminates," *IEEE Trans. Antennas Propag.*, vol. 66, no. 7, pp. 3540-3547, Jul. 2018.

- [47] A. Afsari, A. M. Abbosh, and Y. Rahmat-Samii, "Modified Born iterative method in medical electromagnetic tomography using magnetic field fluctuation contrast source operator," *IEEE Trans. Microw. Theory Techn.*, vol. 67, no. 1, pp. 454-463, Jan. 2019.
- [48] X. Song, M. Li, F. Yang, S. Xu, and A. Abubakar, "Study on joint inversion algorithm of acoustic and electromagnetic data in biomedical imaging," *IEEE J. Multiscale Multiphys. Comput. Techn.*, vol. 4, pp. 2-11, 2019.
- [49] M. Salucci, G. Oliveri, and A. Massa, "Real-Time electrical impedance tomography of the human chest by means of a learning-by-examples method," *IEEE J. Electromagn. RF Microw. Med. Biol.*, vol. 3, no. 2, pp. 88-96, Jun. 2019.
- [50] Y. Chu, K. Xu, Y. Zhong, X. Ye, T. Zhou, X. Chen, and G. Wang, "Fast microwave through wall imaging method with inhomogeneous background based on Levenberg-Marquardt algorithm," *IEEE Trans. Microw. Theory Techn.*, vol. 67, no. 3, pp. 1138-1147, Mar. 2019.
- [51] S. Caorsi, M. Donelli, D. Franceschini, and A. Massa, "A new methodology based on an iterative multiscaling for microwave imaging," *IEEE Trans. Microw. Theory Techn.*, vol. 51, pp. 1162-1173, 2003.
- [52] A. Abubakar, W. Hu, P. M. van den Berg, and T. M. Habashy, "A finite-difference contrast source inversion method," *Inverse Probl.*, vol. 24, 065004, 2008.
- [53] X. Chen, "Subspace-based optimization method for inverse scattering problems with an inhomogeneous background medium," *Inverse Probl.*, vol. 26, 074007, 2010.
- [54] M. Catedra, R. Torres, J. Basterrechea, and E. Gago, *The CG-FFT Method-Application of Signal Processing Techniques to Electromagnetics*. Boston, MA, USA: Artech House, 1995.
- [55] W. C. Chew, J. M. Jin, E. Michielssen, and J. M. Song, *Fast and Efficient Algorithms in Computational Electromagnetics*. Norwood, MA: Artech House, 2001.

- [56] K. Xu, Y. Zhong, X. Chen, and D. Lesselier, "A fast integral equation-based method for solving electromagnetic inverse scattering problems with inhomogeneous background," *IEEE Trans. Antennas Propag.*, vol. 66, no. 8, pp. 4228-4239, Aug. 2018.
- [57] M. Donelli, G. Franceschini, A. Martini, and A. Massa, "An integrated multi-scaling strategy based on a particle swarm algorithm for inverse scattering problems," *IEEE Trans. Geosci. Remote Sens.*, vol. 44, no. 2, pp. 298-312, Feb. 2006.
- [58] G. Oliveri, Y. Zhong, X. Chen, and A. Massa, "Multiresolution subspace-based optimization method for inverse scattering problems," *J. Opt. Soc. Am. A*, vol. 28, no. 10, pp. 2057-2069, Oct. 2011.
- [59] Y. Zhong, M. Salucci, K. Xu, A. Polo, and A. Massa, "A multiresolution contraction integral equation method for solving highly nonlinear inverse scattering problems," *IEEE Trans. Microw. Theory Techn.*, vol. 68, no. 4, pp. 1234-1247, Apr. 2020.
- [60] G. Franceschini, D. Franceschini, and A. Massa, "Full-Vectorial three-dimensional microwave imaging through the iterative multiscaling strategy—a preliminary assessment," *IEEE Geoscience Remote Sens. Letters*, vol. 2, no. 4, pp. 428-432, Oct. 2005.
- [61] M. Donelli, D. Franceschini, P. Rocca, and A. Massa, "Three-dimensional microwave imaging problems solved through an efficient multiscaling particle swarm optimization," *IEEE Trans. Geosci. Remote Sens.*, vol. 47, no. 5, pp. 1467-1481, May 2009.
- [62] X. Ye, L. Poli, G. Oliveri, Y. Zhong, K. Agarwal, A. Massa, and X. Chen, "Multi-resolution subspace-based optimization method for solving three-dimensional inverse scattering problems," *J. Opt. Soc. Am. A*, vol. 32, no. 11, pp. 2218-2226, Nov. 2015.
- [63] M. Conci, M. Donelli, G. Franceschini, and A. Massa, "Microwave imaging from limited-angle scattered data using the iterative multiscaling approach," *Microw. Opt. Technol. Lett.*, vol. 44, no. 4, pp. 358-363, Feb. 2005.
- [64] M. Salucci, C. Estatico, A. Fedeli, G. Oliveri, M. Pastorino, S. Povoli, A. Randazzo, and P. Rocca, "2-D TM GPR imaging through a multiscaling multifrequency approach in  $L^p$  spaces," *IEEE Trans. Geosci. Remote Sens.*, vol. 59, no. 12, pp. 10011-1021, Dec. 2021.

- [65] S. Goudos, *Emerging Evolutionary Algorithms for Antennas and Wireless Communications*. SciTech/IET, 2021 (ISBN-13: 978-1-78561-552-8).
- [66] X. Z. Ye, Y. Zhong, and X. Chen, “Reconstructing perfectly electric conductors by the subspace-based optimization method with continuous variables,” *Inverse Probl.*, vol. 27, no. 5, pp. 055011, May 2011.
- [67] J. Geffrin, P. Sabouroux, and C. Eyraud, “Free space experimental scattering database continuation: experimental set-up and measurement precision,” *Inverse Probl.*, vol. 21, no. 6, pp. 117-130, Nov. 2005.
- [68] Y. Zhong, X. Chen, and K. Agarwal, “An improved subspace-based optimization method and its implementation in solving three-dimensional inverse problems,” *IEEE Trans. Geosci. Remote Sens.*, vol. 48, no. 10, pp. 3763-3768, Oct. 2010.
- [69] G. W. Stewart, *Matrix Algorithms*. Philadelphia, PA: SIAM, 1998.

## FIGURE CAPTIONS

- **Figure 1.** *Problem Scenario* - Contrast distribution (a) without and (b) with the scatterer as well as (c) differential profile.
- **Figure 2.** *Illustrative Example* ( $S = 4$ ) - Evolution of the RoIs ( $\mathcal{S}_{\Delta X}^{(s)}$ ,  $\mathcal{S}_{\Delta J}^{(s)}$ ) at different MS steps: (a)  $s = 1$ , (b)  $s = 2$ , (c)  $s = 3$ , and (d)  $s = S$ .
- **Figure 3.** *Control-Parameters Calibration* (“Square” object [ $\tau_{\Delta} = 2$ ],  $M = V = 27$ , MS-DCIE) - Plots of the total reconstruction error,  $\Xi_{tot}$ , as a function of (a)  $\alpha$  ( $\gamma = 1.4$ ) and (b)  $\gamma$  ( $\alpha = 0.4$ ).
- **Figure 4.** *Numerical Assessment* (“Square” object [ $\tau_{\Delta} = 2$ ],  $M = V = 27$ ,  $SNR = 20$  [dB], MS-DCIE) - Plots of the cost function,  $\Psi$ , the total reconstruction error,  $\Xi_{tot}$ , and the MS zooming factor,  $\eta^{(s)}$ , versus the MS step index ( $s = 1, \dots, S$ ).
- **Figure 5.** *Numerical Assessment* (“Square” object [ $\tau_{\Delta} = 2$ ],  $M = V = 27$ ,  $SNR = 20$  [dB]) - Maps of (a)-(d) the retrieved differential contrast,  $\tau_{\Delta}$ , at different steps of the MS-DCIE [(a)  $s = 1$ , (b)  $s = 2$ , (c)  $s = 3$ , and (d)  $s = 4$ ] and (e)(f) the contrast profile,  $\tau^{opt}$ , reconstructed by (e) the MS-DCIE and (f) the DCIE.
- **Figure 6.** *Numerical Assessment* (“Circular Ring” object [ $\tau_{\Delta} = 2$ ],  $M = V = 27$ ) - Plots of the total reconstruction error,  $\Xi_{tot}$ , versus  $SNR$ .
- **Figure 7.** *Numerical Assessment* (“Circular Ring” object [ $\tau_{\Delta} = 2$ ],  $M = V = 27$ ,  $SNR = 20$  [dB]) - Maps of the local error,  $\mathbb{E}$ , yielded by (a) the MS-DCIE, (b) the DCIE, (c) the MS-DLSIE, and (d) the DLSIE.
- **Figure 8.** *Numerical Assessment* (“Circular Ring” object,  $M = V = 27$ ,  $SNR = 20$  [dB]) - Plots of the global reconstruction errors as a function of the actual differential contrast,  $\tau_{\Delta}$ .
- **Figure 9.** *Numerical Assessment* (“Circular Ring” object,  $M = V = 27$ ,  $SNR = 20$  [dB]) - Maps of the local error,  $\mathbb{E}$ , yielded by (a)(b) the MS-DCIE and (c)(d) the DCIE when (a)(c)  $\tau_{\Delta} = 3$  and (b)(d)  $\tau_{\Delta} = 4$ .

- **Figure 10.** *Numerical Assessment* (“Circular Ring” object [ $\text{Re}\{\tau_\Delta\} = 2$ ],  $M = V = 27$ ,  $SNR = 20$  [dB]) - Plots of the global reconstruction errors as a function of the actual differential conductivity,  $\sigma_\Delta$ .
- **Figure 11.** *Numerical Assessment* (“Circular Ring” object [ $\text{Re}\{\tau_\Delta\} = 2$ ,  $\sigma_\Delta = 10^{-1}$  [S/m]],  $M = V = 27$ ,  $SNR = 20$  [dB]) - Maps of the (a)(c) real and the (b)(d) imaginary part of the local error,  $\mathbb{E}$ , yielded by (a)(b) the *MS-DCIE* and (c)(d) the *DCIE*.
- **Figure 12.** *Numerical Assessment* (“Square” object [ $\tau_\Delta = 2$ ],  $M = V = 27$ ,  $SNR = 20$  [dB]) - Plots of the global reconstruction errors versus the *a-priori* knowledge uncertainty,  $\delta$ .
- **Figure 13.** *Numerical Assessment* (“Square” object [ $\tau_\Delta = 2$ ],  $M = V = 27$ ,  $SNR = 20$  [dB]) - Maps of the local error,  $\mathbb{E}$ , yielded by (a)(c)(e) the *MS-DCIE* and (b)(d)(f) the *DCIE* when (a)(b)  $\delta = 5\%$ , (c)(d)  $\delta = 20\%$ , and (e)(f)  $\delta = 80\%$ .
- **Figure 14.** *Experimental Assessment* (“FoamDielIntTM” object [ $\tau_\Delta = 2$ ,  $\tau_2 = 0.45$ ],  $V = 8$ ,  $M = 241$ ) - Maps of (a) the actual contrast,  $\tau$ , (b) the host medium,  $\tau_H$ , and (c) the actual differential contrast,  $\tau_\Delta$ .
- **Figure 15.** *Experimental Assessment* ( $f = 7$  [GHz], “FoamDielIntTM” object [ $\tau_\Delta = 2$ ,  $\tau_2 = 0.45$ ],  $V = 8$ ,  $M = 241$ ) - Maps of the local error,  $\mathbb{E}$ , yielded by (a) the *MS-DCIE*, (b) the *DCIE*, (c) the *MS-DLSIE*, and (d) the *DLSIE*.
- **Figure 16.** *Experimental Assessment* ( $f = 8$  [GHz], “FoamDielIntTM” object [ $\tau_\Delta = 2$ ,  $\tau_2 = 0.45$ ],  $V = 8$ ,  $M = 241$ ) - Maps of the local error,  $\mathbb{E}$ , yielded by (a) the *MS-DCIE*, (b) the *DCIE*, (c) the *MS-DLSIE*, and (d) the *DLSIE*.

## TABLE CAPTIONS

- **Table I.** *Experimental Assessment* (“FoamDielIntTM” object [ $\tau_\Delta = 2$ ,  $\tau_2 = 0.45$ ],  $V = 8$ ,  $M = 241$ ) - Total reconstruction error,  $\Xi_{tot}$ .

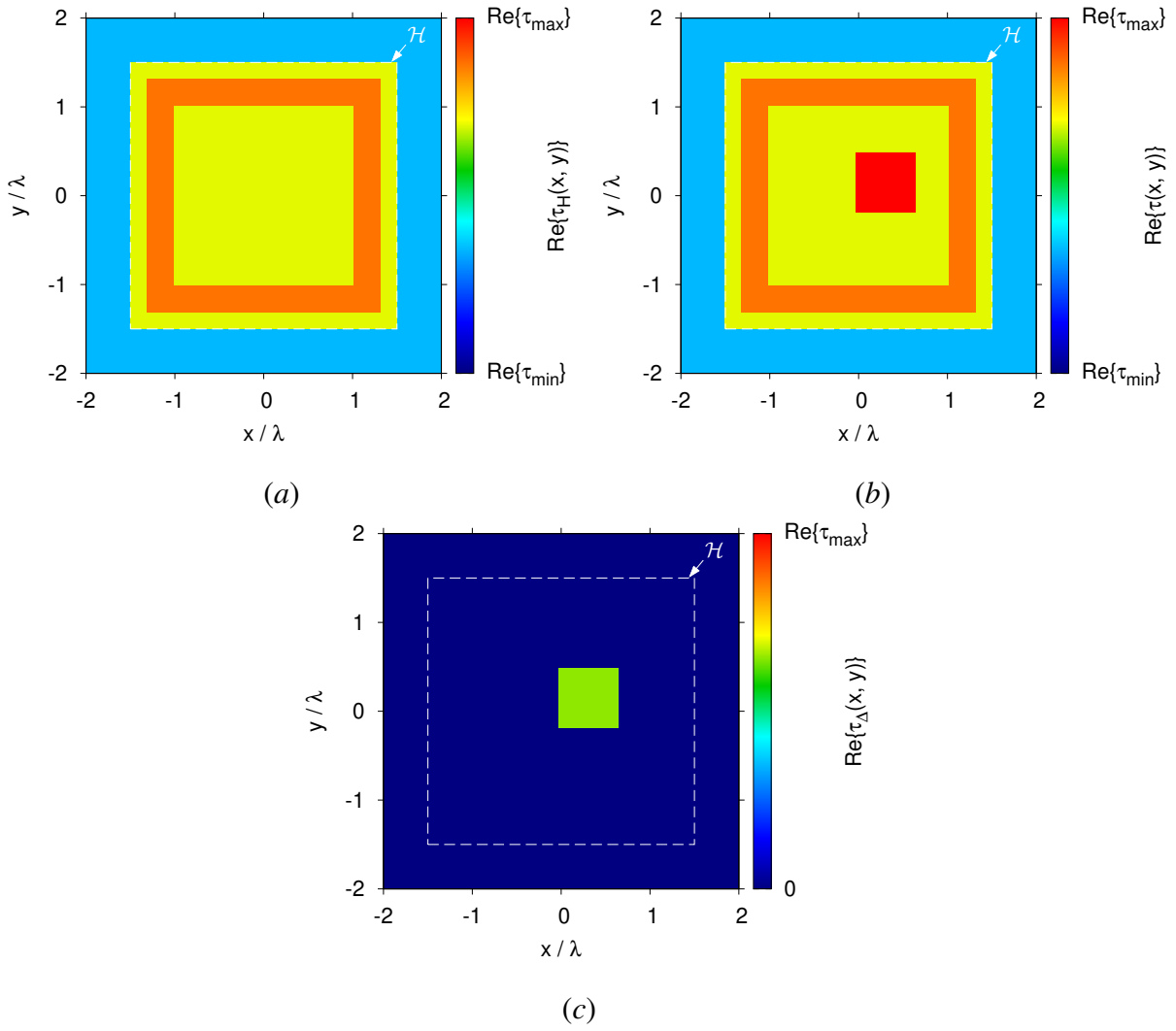


**Fig. 1 - Zhong et al., “Multi-Scaling Differential Contraction ...”**



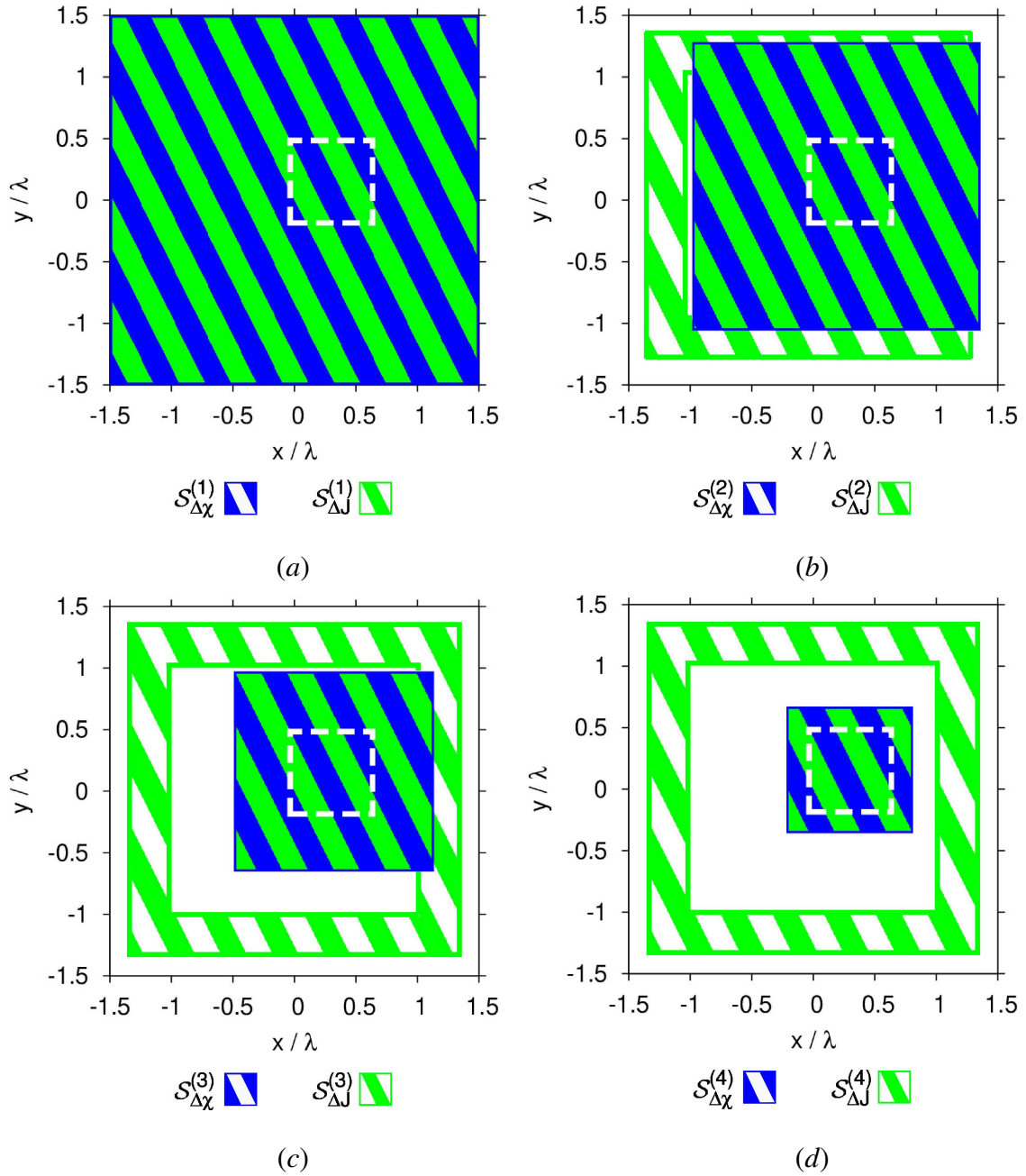
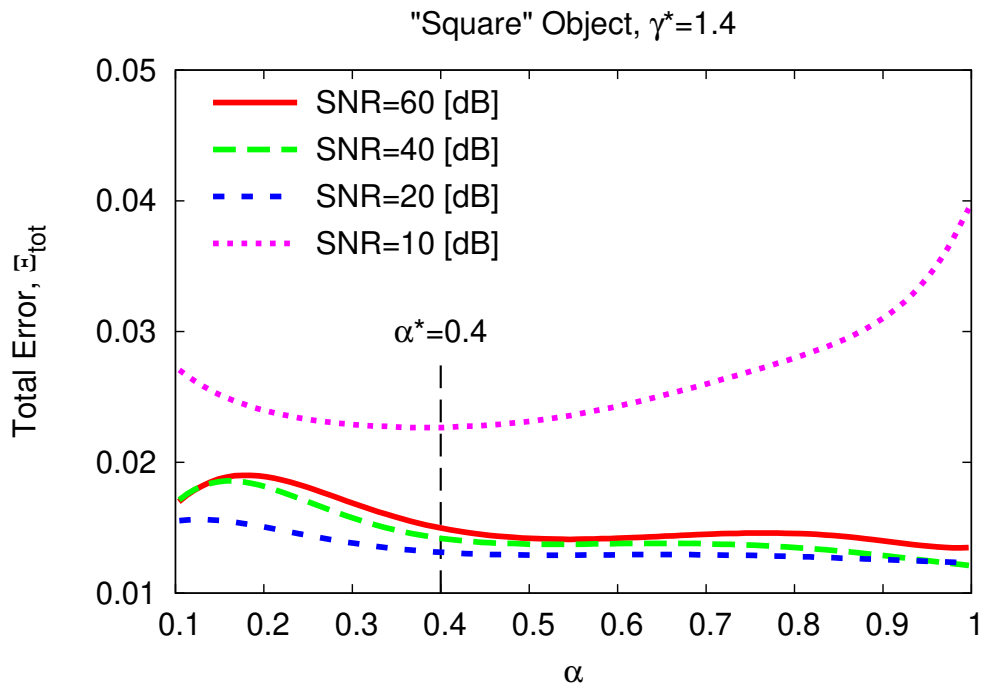
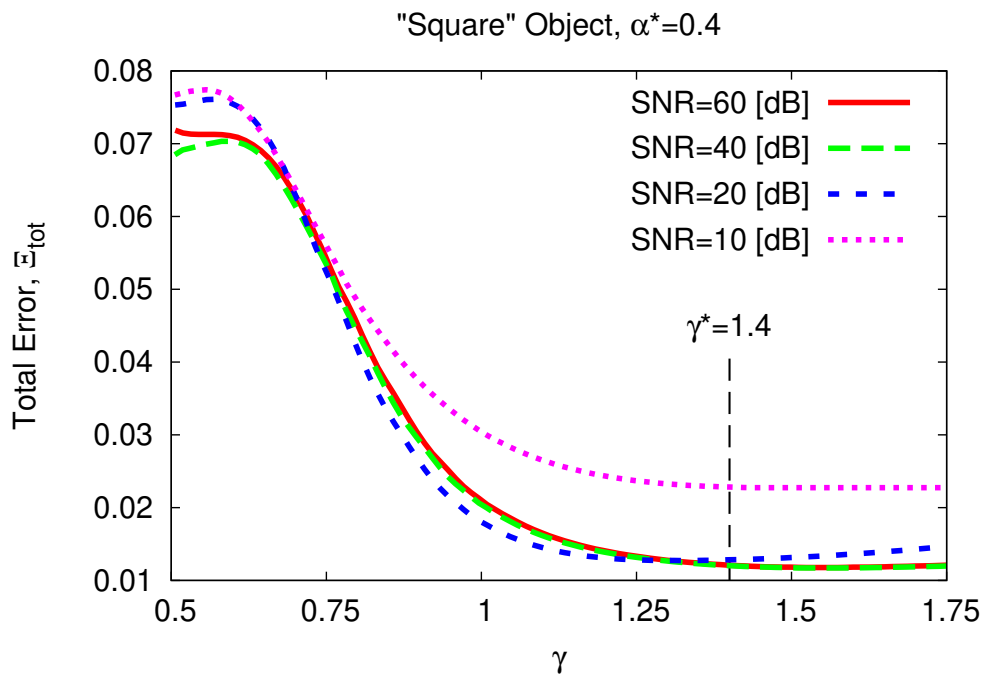


**Fig. 2 - Zhong et al., “Multi-Scaling Differential Contraction ...”**



(a)



(b)

**Fig. 3 - Zhong et al., "Multi-Scaling Differential Contraction ..."**

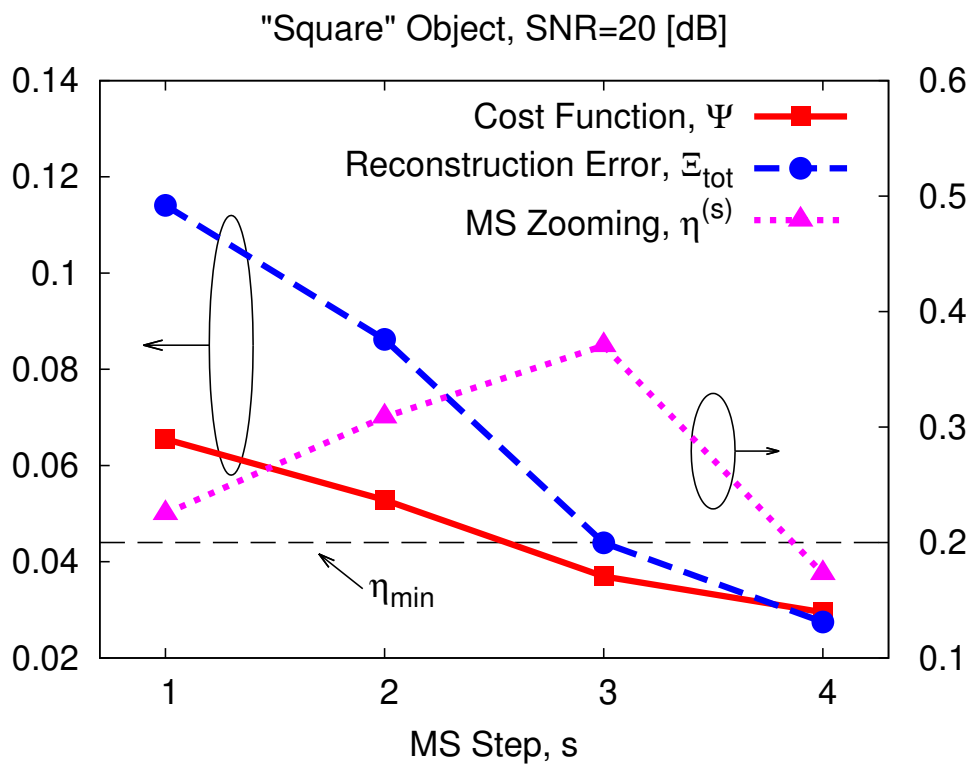


**Fig. 4 - Zhong et al., “Multi-Scaling Differential Contraction ...”**

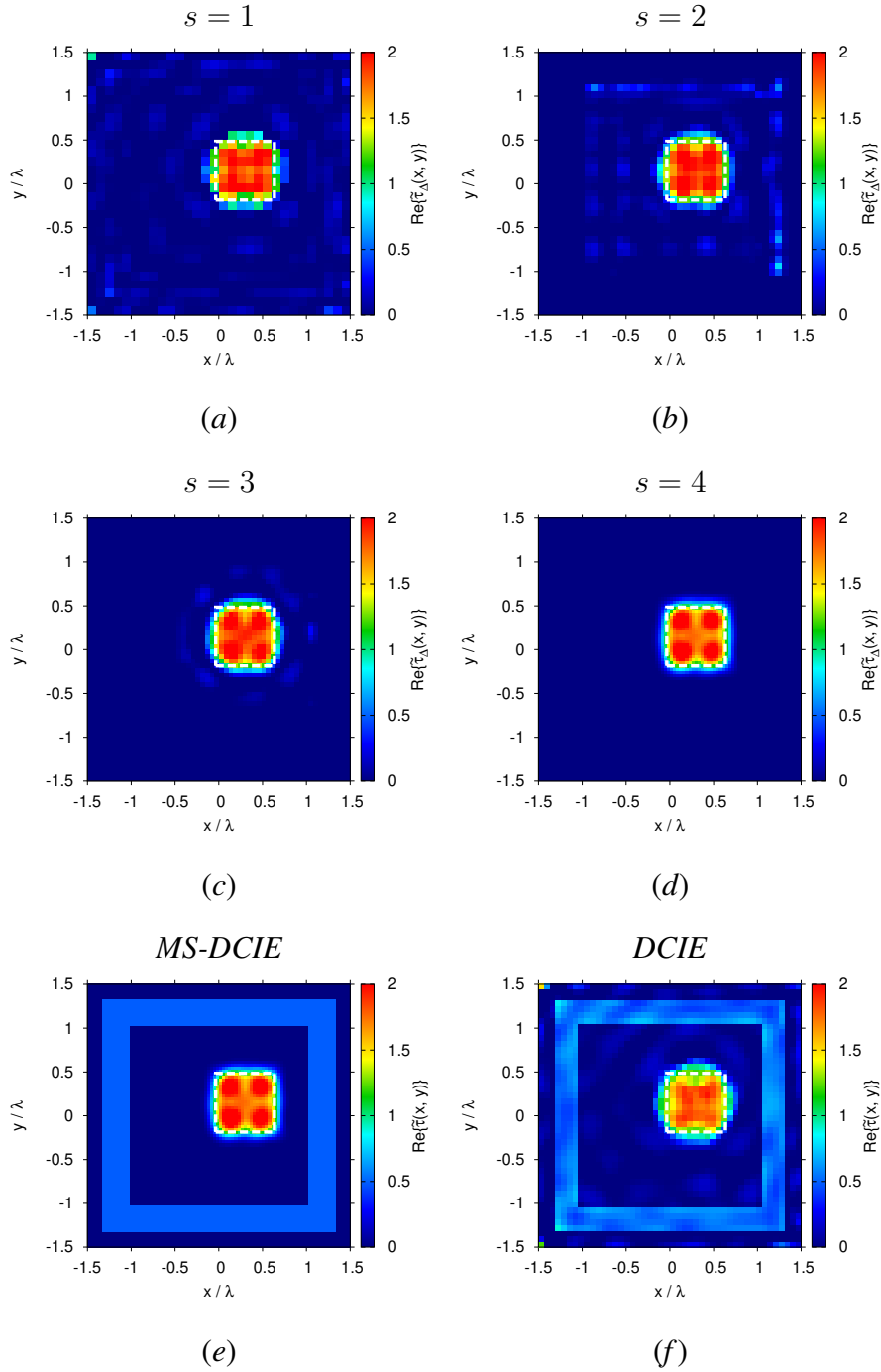
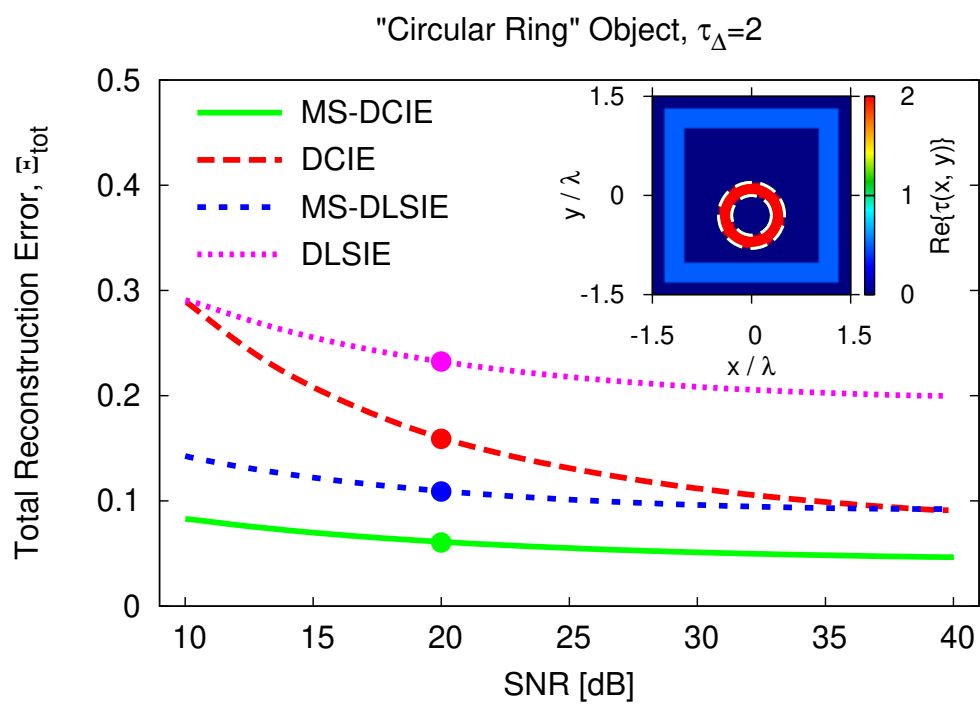
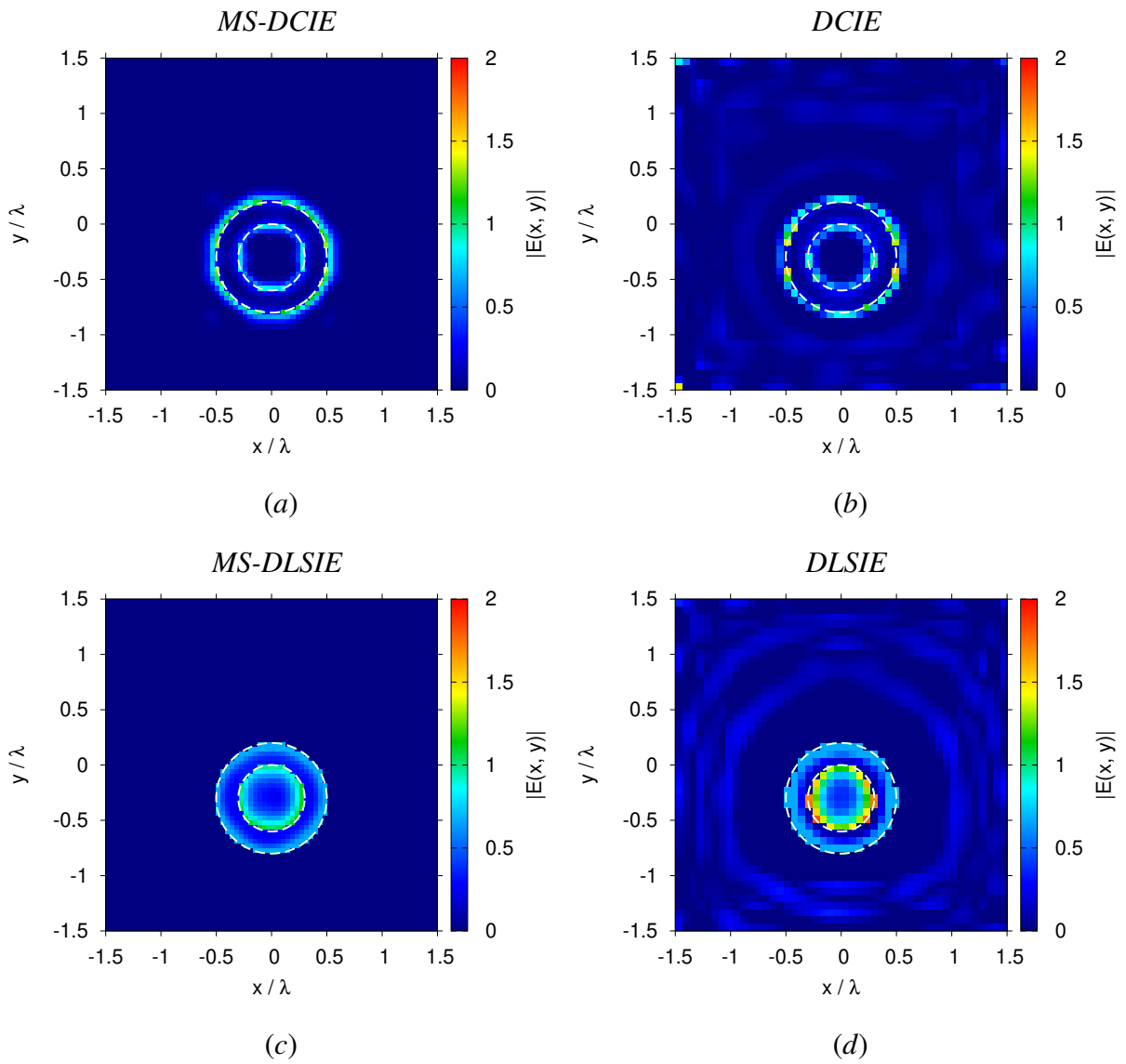


Fig. 5 - Zhong et al., "Multi-Scaling Differential Contraction ..."



**Fig. 6 - Zhong et al., "Multi-Scaling Differential Contraction ..."**



**Fig. 7 - Zhong et al., “Multi-Scaling Differential Contraction ...”**

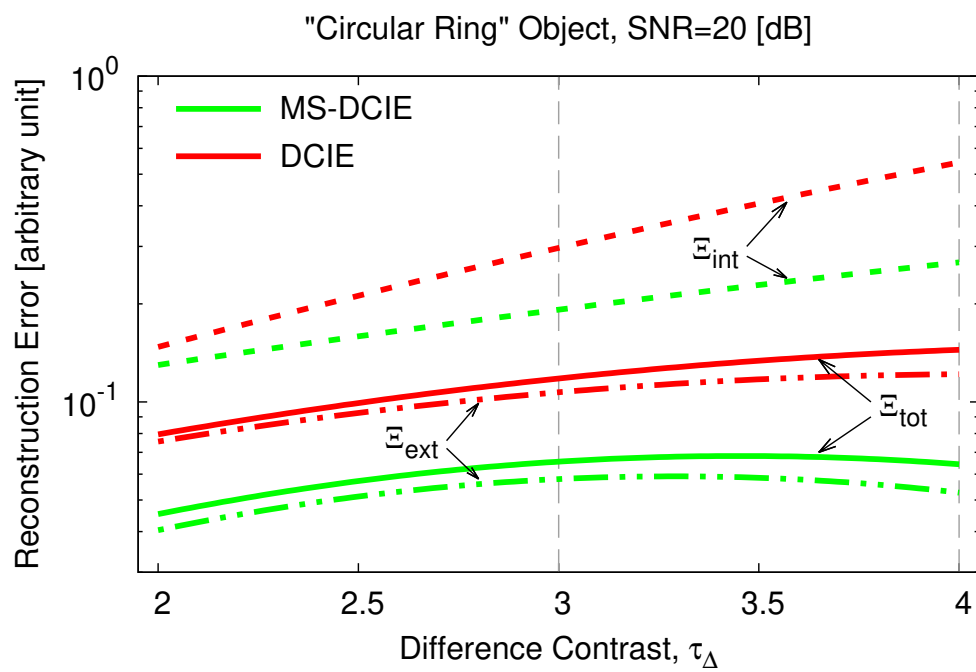


**Fig. 8** - Zhong et al., "Multi-Scaling Differential Contraction ..."

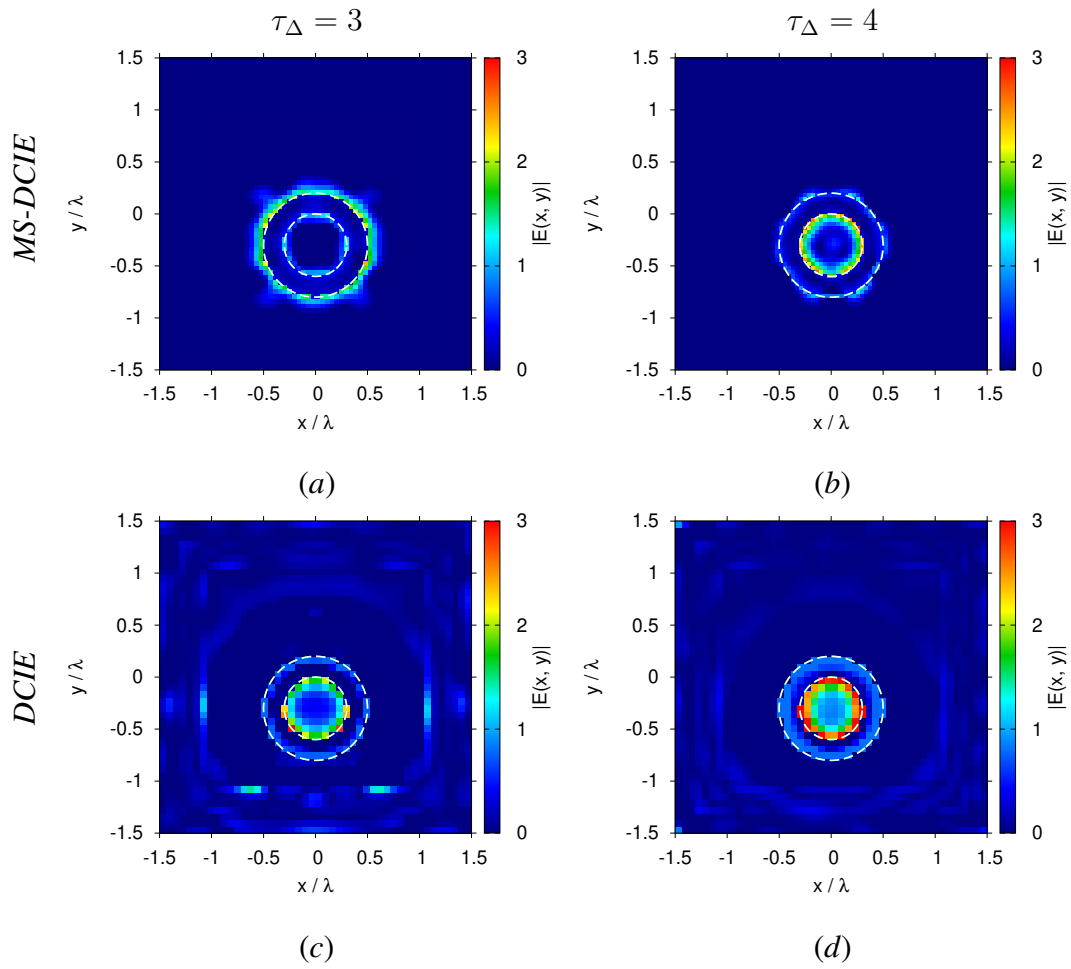


**Fig. 9 - Zhong et al., “Multi-Scaling Differential Contraction ...”**



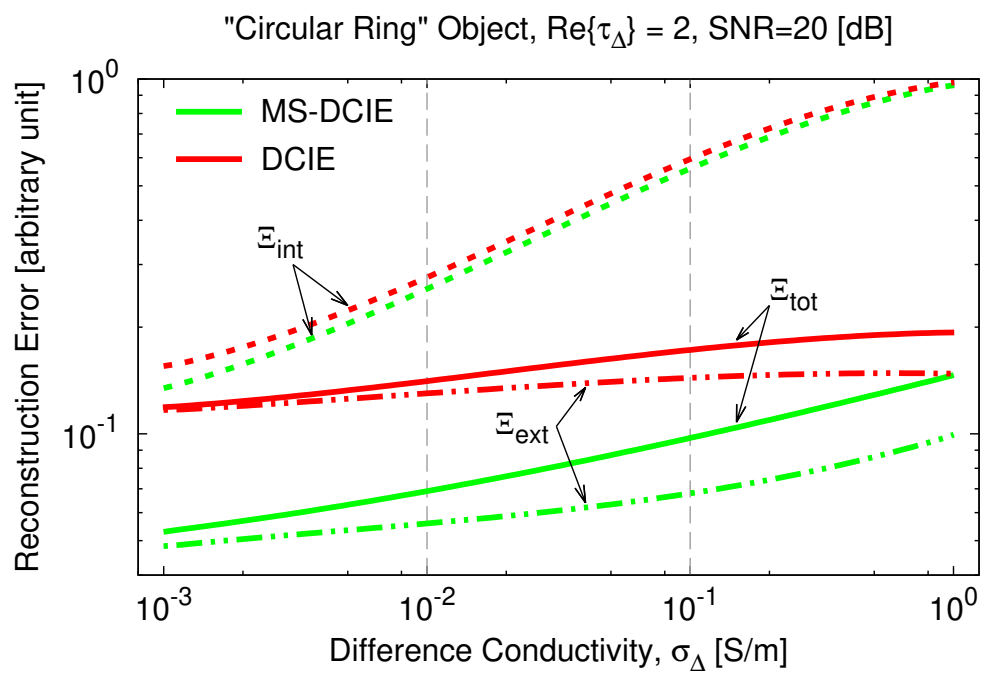


**Fig. 10** - Zhong *et al.*, "Multi-Scaling Differential Contraction ..."

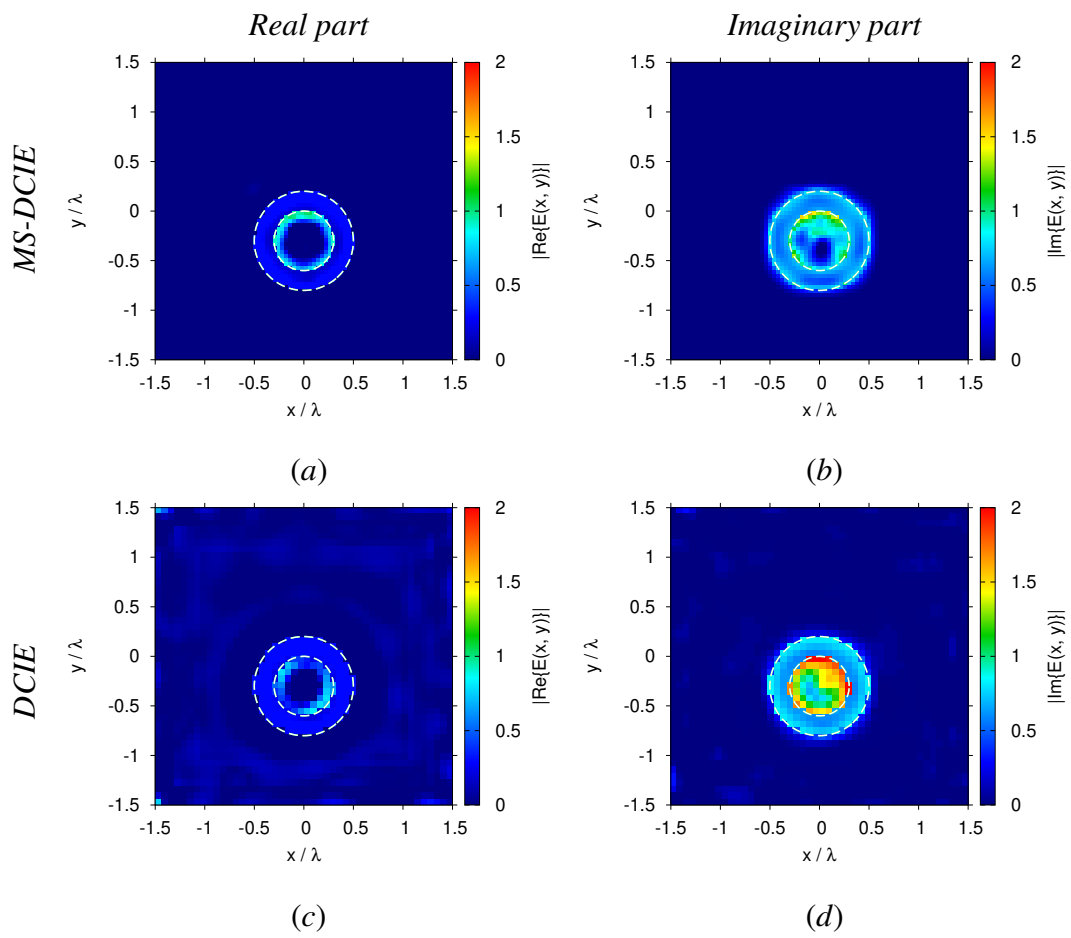


**Fig. 11 - Zhong et al., “Multi-Scaling Differential Contraction ...”**

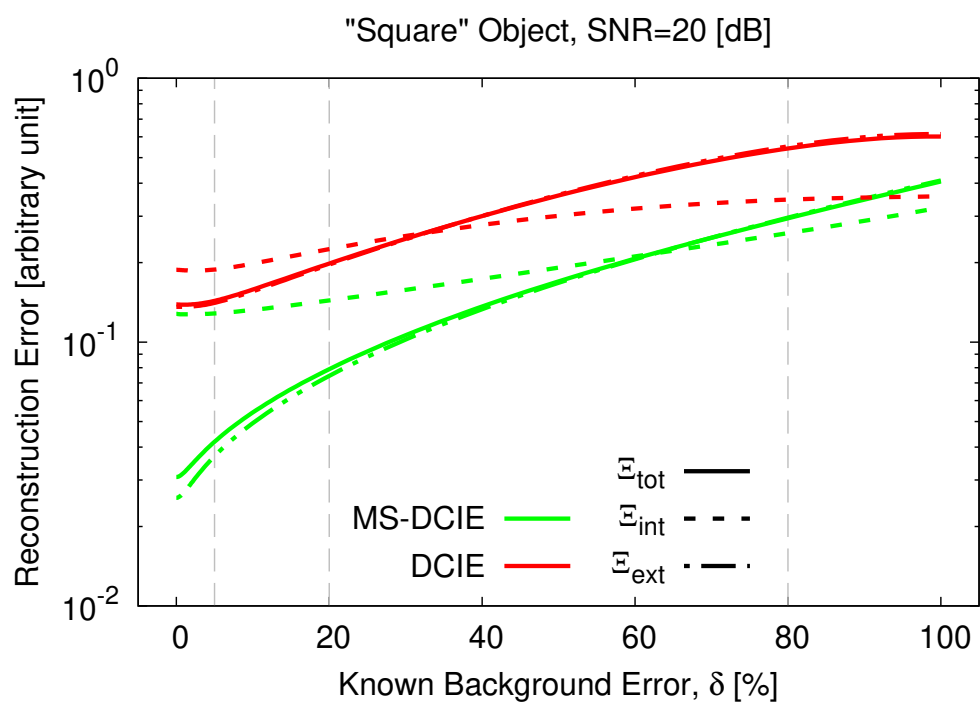


**Fig. 12** - Zhong *et al.*, "Multi-Scaling Differential Contraction ..."

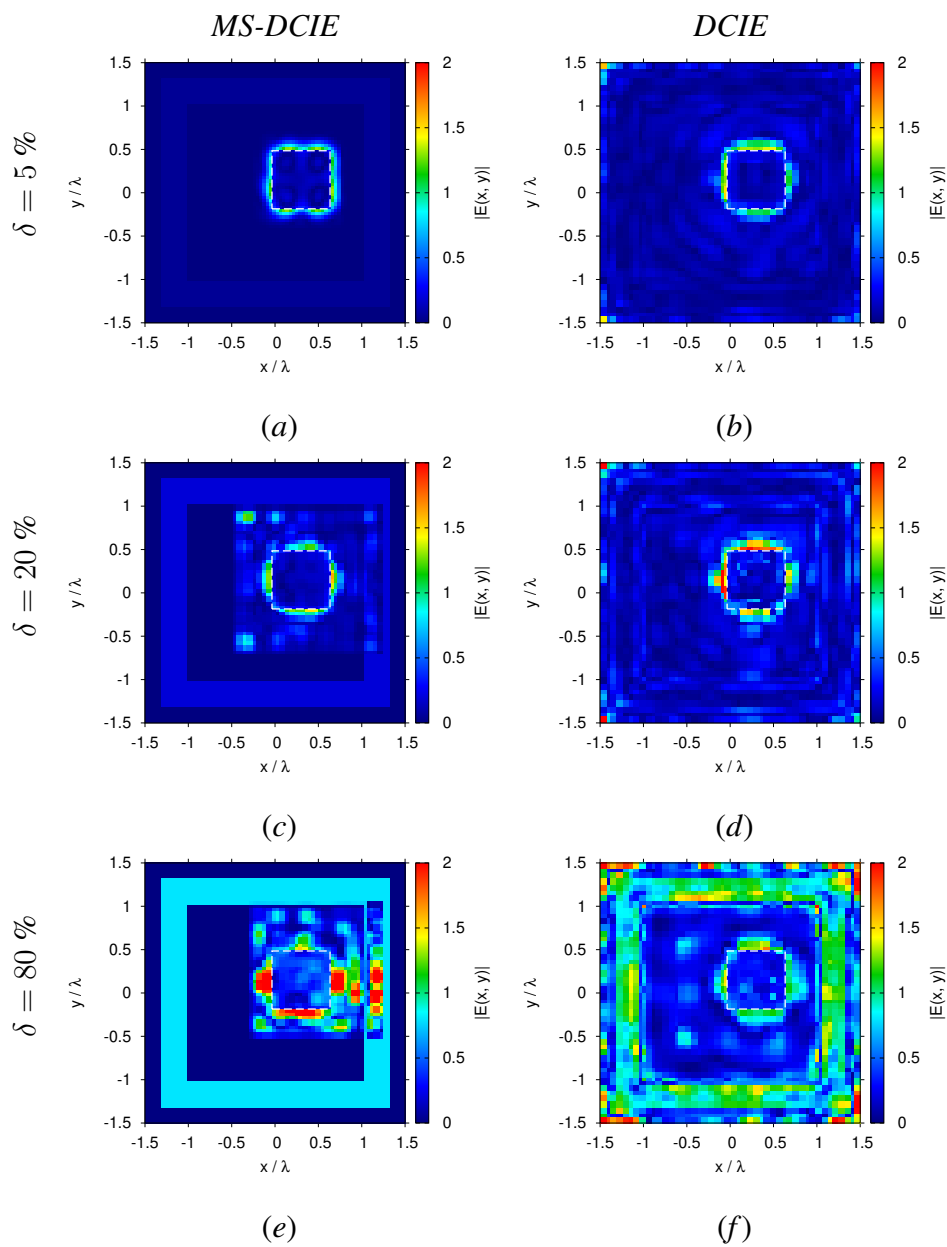


Fig. 13 - Zhong et al., “Multi-Scaling Differential Contraction ...”

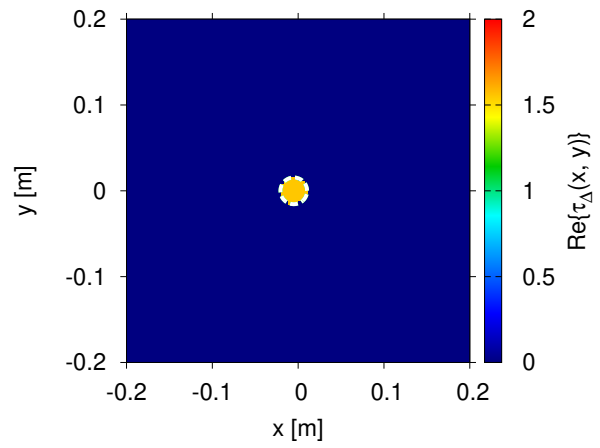
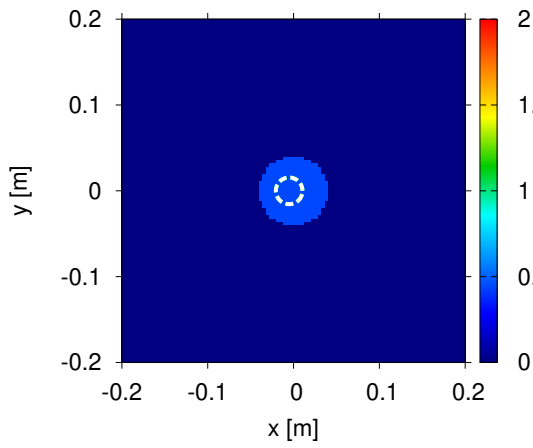
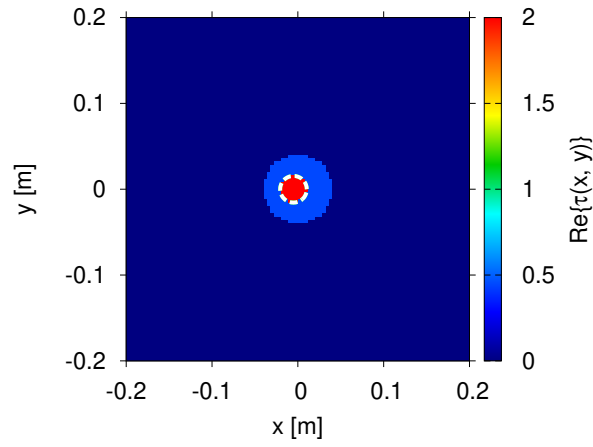
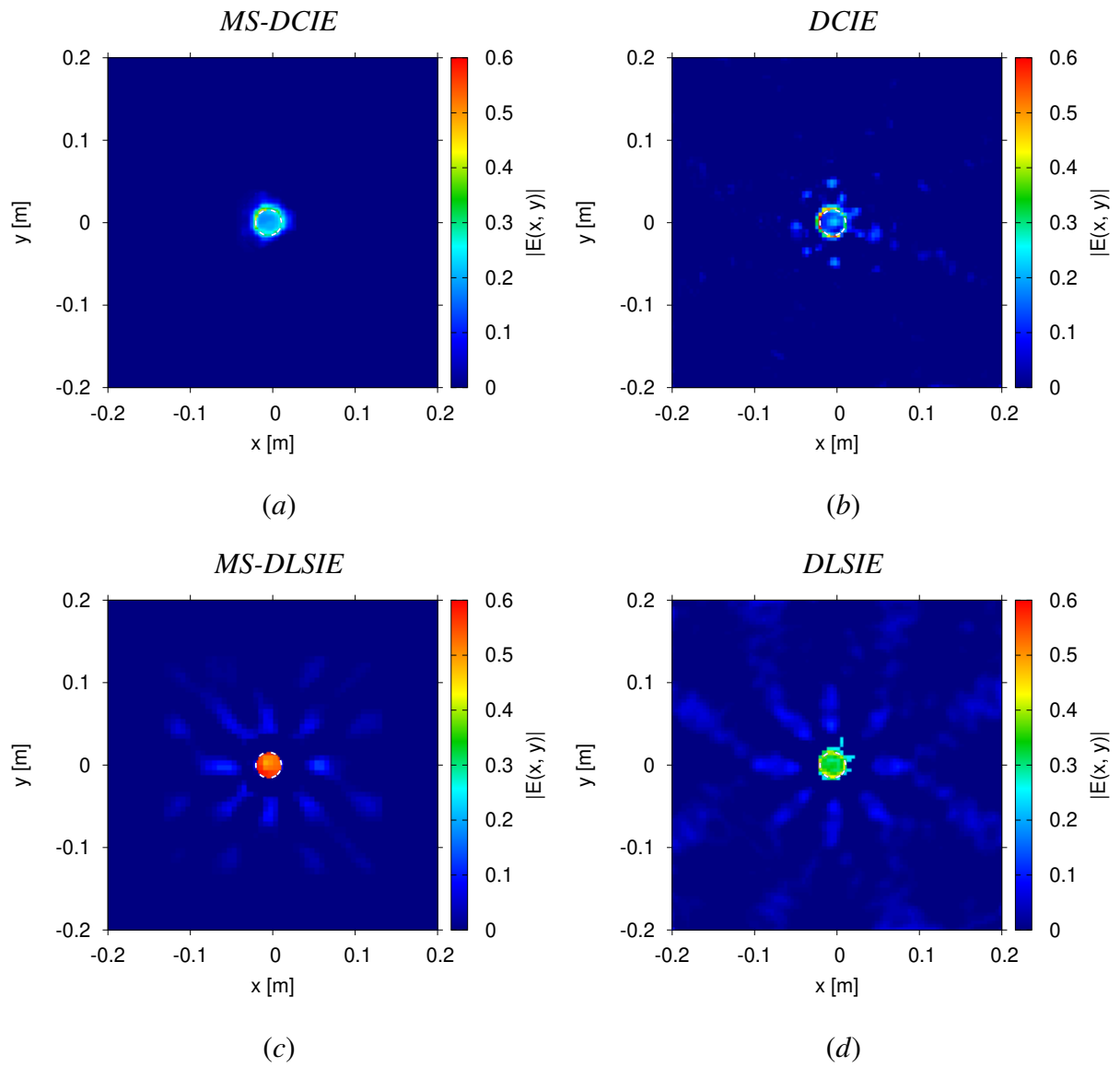
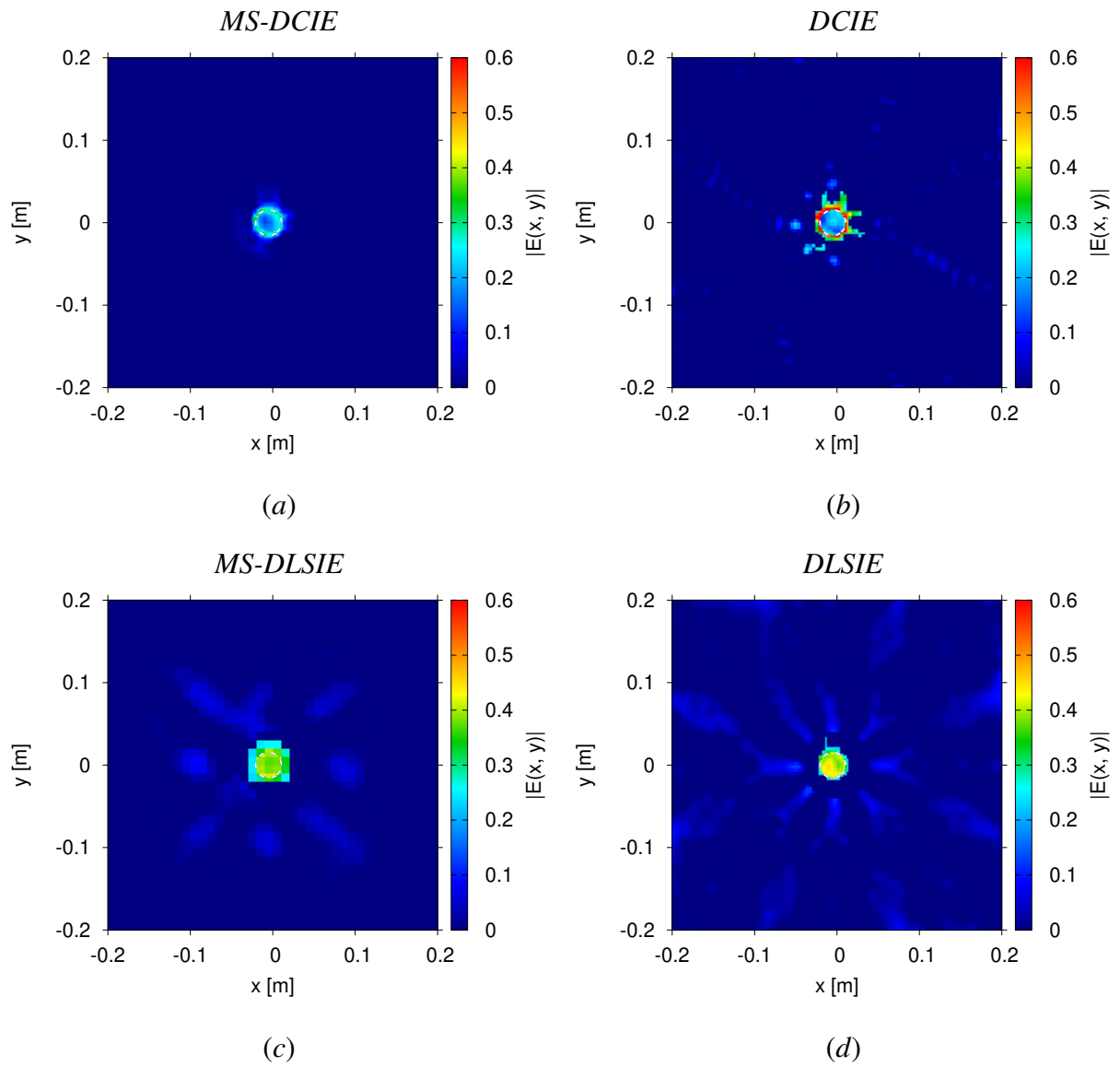


Fig. 14 - Zhong et al., “Multi-Scaling Differential Contraction ...”



**Fig. 15 - Zhong et al., “Multi-Scaling Differential Contraction ...”**



**Fig. 16 - Zhong et al., “Multi-Scaling Differential Contraction ...”**

$f$ [GHz]	$\Xi_{tot} [\times 10^{-3}]$			
	<i>MS-DCIE</i>	<i>DCIE</i>	<i>MS-DLSIE</i>	<i>DLSIE</i>
6.0	4.57	6.39	8.28	12.47
7.0	5.01	6.01	8.31	12.93
8.0	4.69	8.31	10.91	12.32
9.0	4.39	6.70	8.84	11.34

**Tab. I - Zhong et al., “Multi-Scaling Differential Contraction ...”**